Scoping Studies on the Effects of Dopants and Hydrogen on UO_2 Dissolution Rates

Spent Fuel and Waste Disposition

Prepared for
US Department of Energy
Spent Fuel and Waste Science and Technology

Pacific Northwest National Laboratory
SE Asmussen, AP Goulet, and BD Hanson

August 6, 2021
M4SF-21PN010309062
PNNL-31733

SUMMARY

This report discusses the results and conclusions made in FY20 and FY21 at Pacific Northwest National Laboratory (PNNL) in the program focused on the dissolution of UO_2 fuel with various dopants. This report was prepared to support the continuing effort to improve the Fuel Matrix Dissolution Model (FMDM) for use in long-term modeling of spent nuclear fuel (SNF) in a repository. Single pass flowthrough (SPFT) testing was carried out on fuel samples doped with various levels of Ce, Yb, and Nd (1 and 5 at%) in sequential oxidizing and less oxidizing conditions. The less oxidizing conditions were a first scoping test to see how the system performed when sparged with hydrogen gas. Samples were provided by Washington State University (WSU) through a Nuclear Energy University Program (NEUP) partnership.

For Ce doping, it was observed that increasing the Ce content to 5% of the sample slowed the dissolution of the simulated fuel sample. The exception to this was the 1% Ce doped sample at high temperature, which did not show as high resistance to dissolution that the other samples did relative to the pure UO_2. With Nd doping, the fuel dissolution showed clearly that the higher dopant content suppressed sample dissolution. The presence of Yb in the room temperature samples showed only slight suppression of dissolution in comparison to the pure UO_2 sample. However, at the high temperature, a clear trend of dissolution suppression with Yb doping was observed.

Generally, upon switching from oxidizing to less oxidizing conditions, the dissolution rate of the fuel samples decreased, an effect most pronounced at the higher temperature. Investigation of the fuel samples after corrosion showed a preferential grain boundary dissolution on the following samples: pure UO_2 at 75°C, 5% Ce-doped UO_2 at 75°C, 5% Nd-doped UO_2 at 25°C, and the 5% Yb-doped UO_2 at 75°C. Other samples, such as 1% Ce-doped UO_2 at 25°C, 5% Ce-doped samples at 25°C and 75°C, 1% Yb-doped UO_2 at 75°C, 1% and 5% Yb-doped UO_2 at 25°C, showed increased pore sizes post-dissolution as well as some rounded edges. These results help further our understanding of the role of rare earth fission products controlling UO_2 dissolution in oxidizing and less oxidizing conditions.

Future work using the SPFT system includes dopant combinations to determine the effects of multiple species present, increased dopant content, and in particular, the study of simulated fuels containing Cr and/or Al, both combined and separate. Increasing the range of components, temperatures, and environments will help in further understanding the behavior of fuels in a variety of repository conditions. Modifications to the system based on lessons learned from this test will be made to better achieve anoxic or reducing conditions. The results of this work further our understanding of the role of dopants and redox conditions on SNF dissolution. The information will be critical moving forward to improving the FMDM.

This page is intentionally left blank.

ACKNOWLEDGEMENTS

The authors sincerely thank the projects US Department of Energy (DOE) sponsor, Tim Gunter for supporting and funding this work.

Thank you to operations staff and radiation protection at the Radiochemical Processing Laboratory, PNNL, for making this work possible and workable. We would like to specifically thank Paul MacFarlan, Clynt Bohlke, and Kyle Maloy for assisting us when needed and helping us to safely complete this work. Thanks to Liem Dinh for assistance with operations and the KPA analysis, and Ian Schwerdt for completing the pre-dissolution SEM imaging.

We also thank our collaborators John McCloy and Samuel Karcher at Washington State University for providing the samples for dissolution and study.

Thank you to the organizers of the European Commission's Modern Spent Fuel Dissolution and Chemistry in Failed Container Conditions (DisCo) annual meeting for including PNNL in the annual meeting and updates.

This page is intentionally left blank.

CONTENTS

This page is intentionally left blank.

LIST OF FIGURES

LIST OF TABLES

This page is intentionally left blank.

ACRONYMS

BET	Brunauer-Emmett-Teller
CF	cumulative fraction
CF-U	cumulative fraction of uranium
DGR	deep geological repository
DisCo	Modern Spent Fuel Dissolution and Chemistry in Failed Container Conditions
EDS	energy dispersive X-ray spectroscopy
Eh	redox potential
EPMA	electron probe microanalyzer
FMDM	Fuel Matrix Dissolution Model
GDSA	Geologic Disposal Safety Assessment
IE	ion exchange
KPA	Kinetic Phosphorescence Analyzer
NDR	normalized dissolution rate
NEUP	Nuclear Energy University Program
PNNL	Pacific Northwest National Laboratory
R&D	research and development
SEM	scanning electrochemical microscopy
SNF	spent nuclear fuel
SPFT	single pass flowthrough
TGA	thermogravimetric analysis
WSU	Washington State University

This page is intentionally left blank.

SCOPING STUDIES ON THE EFFECTS OF DOPANTS AND HYDROGEN ON UO_2 DISSOLUTION RATES

1. INTRODUCTION

A failed waste package containing spent nuclear fuel (SNF) could be exposed to water present in a repository, leading to water contacting SNF, dissolution of the fuel matrix, and subsequent migration of radionuclides from the SNF into the near field environment. Dissolution of the UO_2 matrix will control the release of many radionuclides from the SNF. The matrix dissolution rate depends on a variety of near field factors (e.g., the redox conditions [1, 2], temperature [3, 4], contacting water chemistry including carbonate content [3-5]) along with properties of the SNF (e.g., composition [4], age [3, 6], irradiation [7]). To ensure the long-term prediction of SNF dissolution behavior in a repository, models are required that can consider all influencing variables. The test effort covered in this report was performed to evaluate the influence of several of these variables (redox conditions, carbonate presence, composition of the fuel, and temperature) on the dissolution of SNF and provide valuable data to support predictive model development.

In the US, most work on degradation of SNF in a repository has primarily focused on unsaturated oxidizing conditions (e.g., those that exist at Yucca Mountain [8]), however other repository designs are possible [3, 9]. For deep geological repositories (DGRs) in other countries, such as Canada, Sweden, and the United Kingdom, reducing conditions will be predominant in the long term [4, 10-13]. In a DGR, oxidizing conditions will initially prevail until the closure of the repository and subsequent consumption of the remaining O_2 present. The sedimentary materials, such as Callovo-Oxfordian clay, and granitic bedrock environments that are planned for use of DGRs in Europe provide low water permeability and reducing conditions, maintaining a low solubility of UO_2 [14].

Regardless of repository type, the conditions within will not be static, and near field conditions will evolve depending on the site. One of the potentially most impactful conditions within the repository for SNF dissolution is the redox conditions. In predominantly reducing conditions the fuel matrix will be in the reduced form, U^{IV}, where UO_2 solubility is low [6]. However, if conditions are more oxidizing solubility of the fuel matrix increases with the appearance of increased oxidation states, e.g., U^{VI} [3]. The difference between presumed dissolution rates of UO_2 in oxidizing and reducing conditions over a range of pH is shown in Figure 1A. The irradiation from the fuel can further compound these influences [15], as radiolysis may create locally oxidizing conditions. Exposed to ionizing radiation, water decomposes into a range of oxidizing (O_2, •OH, HO_2•, H_2O_2) and reducing species ($•e_{aq}^-$, $•O_2^-$, •H). It has been shown that water radiolysis consequently has a significant impact on the dissolution of SNF under oxidizing conditions [3, 7]. The major species that interact with the SNF surface are the molecular products of water radiolysis (H_2O_2, H_2, and O_2) as the radicals formed from radiolysis recombine due to their short lifetimes and reactivity. These molecular products can oxidize U^{IV} to U^{VI}. Understanding the dissolution of SNF under both oxidizing and reducing conditions is crucial for long-term predictive model development.

The chemistry of the contacting water can also influence SNF dissolution, with carbonate being one of the most impactful species and one commonly projected to be present in repositories. Carbonate species in the contacting water would likely increase the UO_2 dissolution rate as bicarbonate/carbonate easily complex with $U^{VI}O_2^{2+}$ and enhance dissolution [4, 16]. This effect is exemplified by the stability diagram of UO_2 in hypothetical repository groundwater, Figure 1B. The water radiolysis product OH• can also generate $CO_3^{\bullet-}$, which is a strong oxidant [4, 16]. Testing in the presence of carbonate species provides highly relevant data for building predictive models.

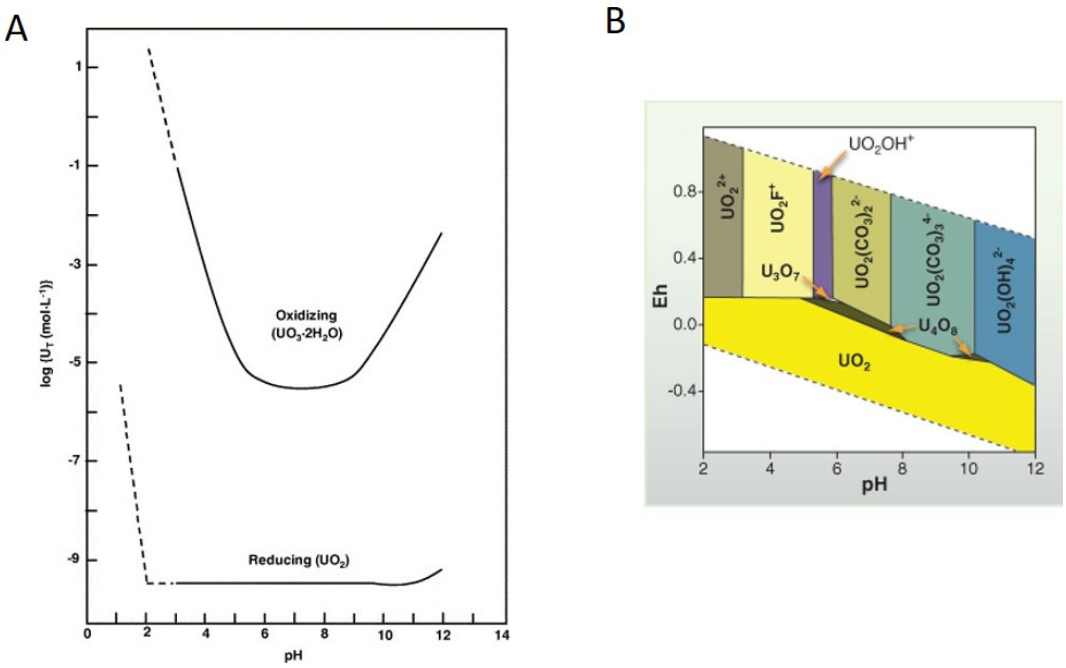

Figure 1. A) A stability diagram for U systems: speciation of U in a hypothetical groundwater at 25°C [17]. B) Solubility of UO_2 and UO_3•$2H_2O$ at 25°C as a function of pH, where U_T is total U [4, 18].

A general assumption of SNF behavior in repository conditions is the dissolution rate would slow with time as the repository temperature decreases, conditions become less aggressive, and fuel chemistry effects dominate[19]. Resulting product concentrations from the radiolysis of species is dependent on the dose rate and energy present. In a gamma field, radicals such as •OH and O_2 form, affecting oxidative dissolution of UO_2. The gamma radiation from the fuel would cease early after disposal. At longer times alpha radiation will be the dominant irradiation source, generating products such as H_2O_2, and in turn affecting UO_2 dissolution rates [4, 20, 21] and formation of alteration products such as studtite [22, 23]. However, H_2O_2 is not as effective in driving fuel matrix dissolution in comparison to radicals formed through gamma water radiolysis; and as such dissolution rates of fuel should decrease with time. Research has focused on using H_2O_2 and/or O_2 as oxidants and to measure the release of U^{VI} with increased time, or to use spent nuclear fuel and to monitor the production of oxidizing species and the dissolved U [4, 5, 24, 25]. However, limited assessments of this hypothesis are available, and trends would be highly dependent on other factors such as fuel composition and the presence of dopants.

For the properties of the fuel itself the reactivity of the UO_2 in the SNF is most affected by rare earth fission product doping of the matrix, non-stoichiometry in the sample, and microstructure [26]. The effect that fission products and actinide-lanthanide doping have on the air oxidation of UO_2 is well studied [6, 27-31]. Typically, UO_2 is oxidized to a final product of U_3O_8, through U_3O_7. With higher dopant amounts (≥4 wt.% to 10wt.%), this process occurs through U_4O_{9+y}, which allows for excess O^{2-} in the matrix; conversion to U_3O_8 from this route is inhibited. As well, trivalent dopants with increasing doping level typically delay UO_2 oxidation by resisting U_3O_8 formation [10, 26, 32]. However, less is known about the role of rare earth fission product dopants in the SNF toward aqueous dissolution and how their overall content influences dissolution. Some trivalent lanthanides, such as Gd, have been extensively studied to understand these impacts [26]. In the case of Gd, increasing dopant concentration increases the number of dopant-oxygen vacancy clusters in the structural matrix [6, 26]. In turn, this decreases the number of oxygen vacancies required to accommodate O ions for oxidation. Similar affects have been observed in Ce dopants as well [33]. However, limited information exists for Ce dopants, and

even less for Nd and Yb dopants [32]. Therefore, understanding the role of all fission products, specifically the Ln^{3+} species, is required to support predictive model develop to adequately represent fuels of varying compositions.

The Fuel Matrix Dissolution Model (FMDM) in the Geologic Disposal Safety Assessment (GDSA) Framework (a repository simulation software tool used to assess geologic disposal of nuclear waste) provides calculations of radionuclide source terms for use in repository performance assessments based on fundamental chemical and physical principles [34]. The model is an electrochemical reaction/diffusion model for the dissolution of used UO_2 developed by Argonne National Laboratory (ANL) and Pacific Northwest National Laboratory (PNNL) that is coded in Matlab [35]. One goal of the GDSA Framework is to study realistic repository simulations to determine areas of needs and uncertainty to aid in research and development (R&D) direction. The FMDM calculates the SNF dissolution rates as a function of radiolysis, alteration layer growth, reactant diffusion through the alteration layer, interfacial corrosion potential, and temperature [36]. Results based on laboratory studies on fuel chemistry in realistic repository environments are important to add to the FMDM to improve fidelity. The results collected in this effort will aid in the simulation of SNF dissolution, especially in the case of the effect of various dopants (e.g. Ce, Nd, Yb at 1at% and 5at%) in the fuel and the influence of changing redox conditions in carbonate containing solutions.

To test the dissolution rates of SNF, a Single Pass Flowthrough (SPFT) system, which has been applied in prior studies of SNF, was utilized in this effort [3, 37-39]. In SPFT leachant passes through a reactor containing crushed (or fragments) of SNF at various rates to achieve a desired saturation level of dissolved species within the reactor. The flow rate : material surface area ratio can be altered by adjusting the flow rate or decreasing the amount of material, resulting in more dilute conditions within the reactor. By increasing the dilution, the solubility of the material in the flow cell (UO_2 in this instance) may increase and prevent back reactions and secondary phase formation. In these dilute conditions the forward, most conservative, dissolution rate of the material can be measured. The rates measured by SPFT from a range of fuel composition samples in both oxidizing and less oxidizing conditions are presented in this effort. These results will help better inform long-term predictive model and assist in improving the FMDM.

This page is intentionally left blank.

2. SINGLE PASS FLOWTHROUGH TESTING

2.1 Test Sample Composition

Doped-UO_2 fuel samples were acquired from Washington State University (WSU) under a Nuclear Energy University Program (NEUP) partnership. Samples received were prepared and sintered at WSU before transfer to PNNL, with samples doped with either Ce, Nd, or Yb, each at a nominal concentration of 1 and 5 at% [32]. A pure UO_2 sample, free of dopants, was also provided for use as comparison to a sample without dopants. Sample composition, as reported by WSU by thermogravimetric analysis (TGA) and electron probe microanalyzer (EPMA, cation analysis), is found in Table 1 [32]. Table 1 shows that the pure UO_2 prepared was slightly hyperstoichiometric, while the samples prepared with dopants were hypostoichiometric; this is important as it does, and did, impact the dissolution rates observed.

Table 1. Composition of the simulated doped UO_2 samples used in this test effort [32].

Sample Description (at %)	Initial Composition	Fraction Uranium (wt%)	U-235 Enrichment
Pure UO_2	$UO_{2.03}$	87.99	0.3%
1% Ce-doped UO_2	$U_{0.988}Ce_{0.012}O_{1.98}$	87.58	0.3%
5% Ce-doped UO_2	$U_{0.947}Ce_{0.053}O_{1.96}$	85.32	0.3%
1% Nd-doped UO_2	$U_{0.985}Nd_{0.015}O_{1.97}$	87.44	0.3%
5% Nd-doped UO_2	$U_{0.948}Nd_{0.052}O_{1.98}$	85.21	0.3%
1% Yb-doped UO_2	$U_{0.982}Yb_{0.018}O_{1.98}$	87.04	0.3%
5% Yb-doped UO_2	$U_{0.947}Yb_{0.053}O_{1.92}$	84.96	0.3%

2.2 Sample Preparation

Single pass flowthrough tests were performed using powdered samples. To generate the powder required for the flow cells, samples were individually ground by mortar and pestle. The ground powder was then placed on a vibratory shaker/tapper sieve system consisting of a 25 µm sieve, a 10 µm sieve, and a catch pan. The sample was sieved until an adequate amount of sample was obtained, nominally 200 mg of powder per sample per flow cell. Powder collected between the two sieves was used for analysis. Samples were not washed prior to sample analysis so as not to alter the powders and prevent oxidation.

A single test case using larger fragment samples was performed using the 5% Ce-doped UO_2 sample. This sample was selected because it had the highest amount of sample available, and most intact pieces. The same number of fragments were collected for two columns to generate comparable results between the two temperatures tested.

Details of samples loaded into the flowcells, including fuel size and specific sample characteristics, are listed in Table 2.

Table 2. Sample loading IDs, dopants, mass, and surface area.

Column	Sample	Fuel Sample Size (g)	BET Surface Area (m^2/g)	U Content	Grams U (g)
A1	Pure UO_2	0.0975	*0.2742**	87.99%	0.0859
A2	1% Ce Doped UO_2	0.1627	0.2697	87.58%	0.1425
A3	5% Ce Doped UO_2	0.1629	0.2022	85.32%	0.1389
A4	1% Nd Doped UO_2	0.2022	0.3032	87.44%	0.1749
A5	5% Nd Doped UO_2	0.2055	0.3136	85.21%	0.1670
A6	1% Yb Doped UO_2	0.1484	0.2722	87.04%	0.1282
A7	5% Yb Doped UO_2	0.1863	0.2844	84.96%	0.1507
A8	5% Ce Fragments	0.2592	0.0118	85.32%	0.2211
B1	1% Ce Doped UO_2	0.2075	0.2697	87.58%	0.1829
B2	Pure UO_2	0.1229	*0.2742**	87.99%	0.1076
B3	5% Ce Doped UO_2	0.2014	0.2022	85.32%	0.1718
B4	1% Nd Doped UO_2	0.2054	0.3032	87.44%	0.1777
B5	5% Nd Doped UO_2	0.203	0.3136	85.21%	0.1650
B6	1% Yb Doped UO_2	0.1471	0.2722	87.04%	0.1271
B7	5% Yb Doped UO_2	0.1981	0.2844	84.96%	0.1602
B8	5% Ce Fragments	0.1666	0.0141	85.32%	0.1421

* Minimum sample required for BET was not obtained. The SA value resulted from an average of all the U containing powder samples to obtain an estimate of specific SA.

The A columns were run at ambient temperature (~25°C) whereas the B columns were run at ~75°C.

Prior to loading into the flow cells, scanning electron microscopy (SEM) was performed on the powder samples to study the grain size and for the presence of remaining fines using the SNE-4500M Plus Tabletop SEM (Nanoimages), Figure 2. On select samples, using a Bruker XFlash 630 attached accessory, Energy Dispersive X-ray Spectroscopy (EDS) was collected to determine the surface composition of the fuel. The EDS is sensitive to approximately 0.5 wt% of a desired element in the material's composition. Surface area measurements were obtained using the Brunauer-Emmett-Teller (BET) method using a Tristar II Plus BET analyzer (Micromeritics), Figure 3.

The specific surface area for most of the spent fuel powders tested under alkaline conditions as reported in previously were in the range 0.0678 – 0.136 m^2/g [8]. The powders used for the acidic tests were prepared similarly to the method presented above and had a specific surface area of 0.28 – 0.29 m^2/g [39]. Casella et al. [3] reported specific surface areas in the range 0.144 – 0.203 m^2/g for powders prepared similarly from pellets of various Gd_2O_3-doping procured from a commercial fuel vendor.

Figure 2. The SNE-4500M Plus Tabletop SEM instrument.

Figure 3. Micromeritics Tristar II Plus analyzer for Brunauer-Emmett-Teller (BET) measurements.

2.3 SPFT Test Apparatus

Oxidative and less oxidizing conditions were tested in flow cells using the PNNL SPFT set up and system. Each SPFT system includes a mobile cart that contains recirculation pumps, pre-equilibrated leachate transfer pumps, a temperature-controlled water bath, and pre-equilibration and feedstock leachate vessels, Figure 4. Both pH and O_2 probes are operated on the system to constantly monitor oxygen content and pH of the leachate. Gas was sparged into the feedstock leachate and leachate equilibration vessels to achieve the desired oxygen content.

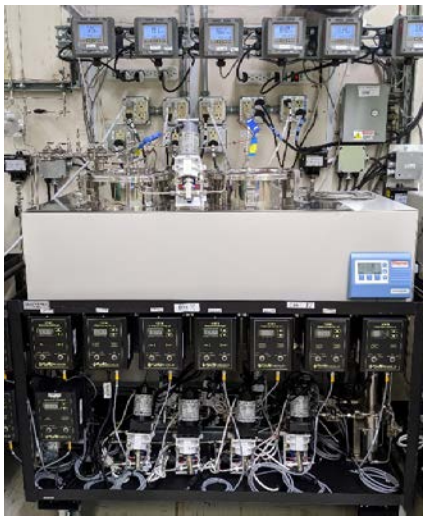

Figure 4. The mobile cart containing the recirculation pumps, pre-equilibrated leachate transfer pumps, temperature-controlled water bath, and pre-equilibration and feedstock leachate vessels. Pictured above the cart is the pH sensor read-out and controller.

Leachate solution travels from the equilibrated temperature baths to the temperature-controlled ovens that contain the flow cells loaded with UO_2 and doped-UO_2 samples, Figure 5. Tubing from each cart travelled into an oven, contained within a ventilated canopy, with each pump corresponding to only one flow cell. The $1/16^{th}$ inch stainless-steel tubing lines between the baths and ovens were not heated or insulated, though the properties of the leachate should not be affected in the stainless-steel lines over the duration of this transport. In the oven, the leachate travelled through coiled tubing below the column containing a fuel sample, which allowed the solution to equilibrate with the test oven temperature prior to contacting the fuel, Figure 6.

Figure 5. The ventilated canopy housing the oven, effluent taps, and funnels directing leachate to ion exchange columns before proceeding to waste.

Figure 6. Flow cells within the oven in a ventilated canopy.

Flow cells that contained the fuel samples were 2 inches long with a 0.24-inch inner diameter. Made of stainless steel, each end was capped with 0.5 µm stainless steel frits to prevent particulate from exiting the columns. Leachate solution entered the flow cells at the bottom and flowed up to prevent air pockets from forming in the flow cells.

After exiting the flow cells, the effluent could travel one of two pathways: the first pathway was through collection taps that allowed for effluent sample collection to determine dissolution rates, and the second through ion exchange (IE) columns before collecting effluent for waste disposal. The IE columns were packed with AG-MP 1M (Bio-Rad Laboratories, Inc.), converted to the carbonate form. This IE media captured the U while allowing the bicarbonate solution to collect in effluent waste containers.

Periodically during testing, the frits or pumps required maintenance due to clogging of the frits. This clogging was a result of two factors: the initial frits had not been cleaned with acetone to remove machining oil, and these samples had more fines that weren't removed via the sieving process compared to the Casella et al. [3] samples as evidenced by the higher specific surface area. Appendix A details the occurrences of this, including any loss of sample mass that occurred when the frits were replaced.

During the experiment, effluent from the SPFT flow cells was collected periodically and analyzed using a Kinetic Phosphorescence Analyzer (KPA, Chemchek Instruments, Inc.) to determine U concentrations, Figure 7. Results allowed for testing of the cumulative fraction of U (CF-U) released from samples as well as the normalized dissolution rate (NDR). As outlined in Hanson and Stout, the cumulative release fractions often show trends that are not as clear when looking at NDR [40].

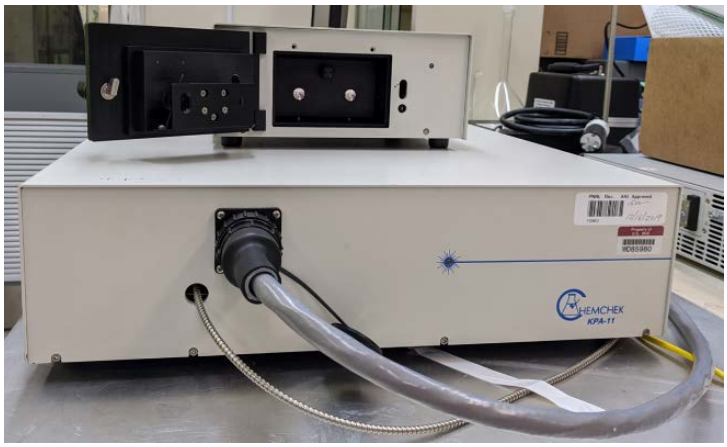

Figure 7. Chemchek Kinetic Phosphorescence Analyzer (KPA) instrument with remote attachment.

Samples were collected for nominally 60 minutes (documented each collection) twice weekly from each of the samples. Solution collected had already flowed through the flow cells and come into contact with the fuel samples. Using KPA, the U concentration of samples was measured and used to calculate the NDR and the CF-U released from the samples using equations 1, 2, and 3.

$$NDR = \frac{(Flow\ Rate)\times(U\ Concentration\ in\ Leachate)}{(Fuel\ Sample\ Size)\times\left(\frac{grams\ U}{grams\ UO_2+Dopant}\right)\times(Specific\ SA)} \quad \textbf{Equation 1}$$

$$CF_x = (U\ Fraction)\times(Day_x - Day_{x-1}) + CF_{x-1} \quad \textbf{Equation 2}$$

$$U\ Fraction = \frac{(Flow\ Rate)\times(U\ Concentration\ in\ Leachate)}{(Fuel\ Sample\ Size)\times\left(\frac{grams\ U}{grams\ UO_2+Dopant}\right)} \quad \textbf{Equation 3}$$

In equations 1 through 3, SA is the specific surface area of the sample (measured by BET), U Fraction is the fractional release of U over a given time period, Day_x is the day number of the sample collection during the run, Day_{x-1} is the prior collection day, CF_x is the cumulative fraction on a given day, CF_{x-1} is the CF of the prior collection, and the (grams U)/(grams UO_2 + Dopant) is the specific fraction of U in the sample which accounts for any dopant weight.

For the first test, lasting 102 days, sparge gas simulated an oxidative environment. From days 102 to 165 the sparge gas was changed for a second test to simulate a reducing (less oxidizing) environment to the best of the system's ability, given the limitation of using at most 5% H_2 because of flammability concerns in a radiological laboratory.

The flow rate of the pumps was set to maintain 0.20 mL/min. However, although the system pumps were calibrated to this flow, this was not always achieved due to clogging of the frits and back pressure of the system, resulting in lower flow rates.

Leachant solution was 2×10^{-3} M sodium bicarbonate in deionized water with a pH maintained between 7 and 8.5. Sparge gas for test one was 20.9% O_2, 2000 ppm CO_2 with a balance of N_2. Test two, which commenced at day 102 without changing the flow cell samples, was 5% H_2 with a balance of N_2. Two temperature set points were analyzed; oven A (flow cells A1 through A8) maintained at room temperature (20°C to 25°C), while oven B (flow cells B1 through B8) was set to 75°C. Pre-equilibration tanks were set to 25°C for both carts A and B due to experimental error; cart B should have been maintained at 75°C. Due to the location of the O_2 probes, the O_2 content was measured coming out of the equilibrated leachate feedstock tank, which was maintained at 25°C. During test one at 25°C the O_2 content fluctuated around 8 ppm to 9.5 ppm. However, based on Henry's Law, the maximum O_2 content at 75°C would be

approximately 4 ppm to 5ppm. Thus, it is likely that the O_2 content in oven B was lower than that in the measured feedstock tank as the oxygen would degas from the leachant as it was heated to 75°C. However, prior studies on the system showed that due to the stainless steel tubing that fed the flow cells in ovens within the canopy enclosure, there was no loss or gain of O_2 concentration, despite any temperature fluctuations that may occur during transport [41]. The full matrix is shown in Table 2.

Test two was the first attempt at producing less oxidizing conditions in this SPFT apparatus. While the oxygen content of the leachant decreased to between 1 to 3.5 ppm, it was not possible to achieve even anoxic conditions because higher concentrations of H_2 were not allowed. Future testing and system modification will be performed to better produce anoxic and reducing conditions.

The mass loaded into the flow cells, as well as the measured specific surface area, U content, and grams of uranium in the sample are presented in Table 2. For the powder samples the specific surface area was measured by the BET instrument. However, due to the low surface area of the fragments, dimensions of those samples were measured using calipers, and then multiplied by a surface roughness factor of 15 [3].

2.4 Post Test Analyses

At the conclusion of the experiment the system was stopped, and the flow cells were allowed to dry. Samples of the material contained within the flow cells were removed to perform SEM and EDS. Unfortunately, due to the small sample size, BET could not be performed on the samples. The SEM imaging was performed at 15 kV accelerating voltage using the secondary electron detector. Individual points of interest were chosen for EDS based on surface features, orientation of sample relative to the detector, and with consideration for charging effects.

This page is intentionally left blank.

3. RESULTS

3.1 Pure UO_2

3.1.1 Pure UO_2 SPFT Tests

Single pass flowthrough tests on pure UO_2 were run in powder form at 25°C and 75°C, oven temperature. The tests began in oxidizing conditions (test 1 – days 0 to 102 with O_2 concentrations ranging from 8.5 to 9.5 ppm) then at day 102 until the end at day 165 (test 2) the sparge gas was changed to 5 % H_2 in N_2, attempting to simulate less oxidizing conditions. After the gas purge the measured O_2 concentration dropped to between 1 to 3.5 ppm. The resulting NDR and CF-U of the samples are shown in Figure 8A and Figure 8B, respectively. The pure UO_2 sample, flowcell A1, in the 25°C flow cell had an initially high NDR that tapered off within approximately 20 days of the system operating. This behavior was attributed to the dissolution of the fines present as the samples were not washed to maintain the sample oxidation state integrity pre-test. Following this, the NDR remained relatively consistent for the rest of the experiment. At 25ºC a slow increase in CF-U was observed. Under the oxidizing conditions of test one, the surface of the powders will be oxidized. Even when the sparge gas was changed, the oxidized surface will dissolve faster than if the sample had been under anoxic/reducing conditions the entire time. Because the conditions of test two were not even fully anoxic, the observed dissolution rates at 25°C remained relatively consistent.

In contrast, the NDR of the 75°C pure UO_2 sample varied significantly over the course of the entire test range, both in the oxidative and less oxidative environment, with only two steady-state-like conditions observed. In turn, a steep trend on the CF-U was observed over the duration of the experiment as expected with the increased temperature and oxidized sample surface.

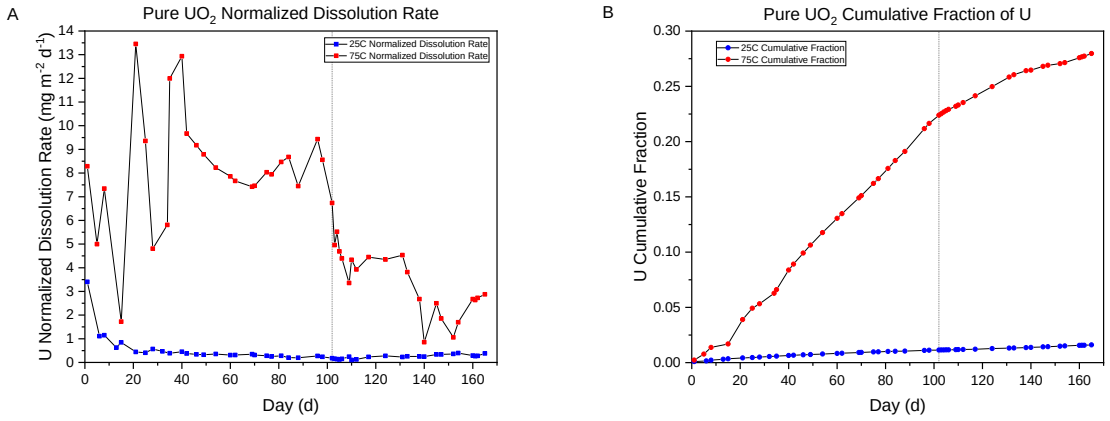

Figure 8. A) The Normalized Dissolution Rate (g m^{-2} d^{-1}) and B) Cumulative Fraction of U for pure UO_2 at 25°C (blue) and 75°C (red).

The conversion of the sparge gas to less oxidizing conditions at day 102 caused the NDR of the 25°C sample to initially fluctuate, and then have an unexplained slow increase beginning at day 120. The NDR after this point at 25 ºC was similar to the fully oxidizing conditions. Conversely, the introduction of less oxidizing conditions for the 75°C sample did not vary as much as the 25 ºC. The NDR at 75 ºC had a slow downward trend after less oxidizing conditions were introduced. This behavior was expected as less oxidizing conditions decrease the likelihood of U dissolution. The effect of less oxidizing conditions was more prominent at 75 ºC due to the higher dissolution rate at higher temperatures, which decrease the effect of the oxidized sample surface.

3.1.2 Pure UO_2 Solids Analysis

The SEM micrographs taken prior to dissolution testing show the sample is of variable size, with a large amount of material below the 10 µm limit that the sieve was supposed to remove, Figure 9A and B. This small-sized material and fines contributed to the clogging of the frits and varied NDR initially seen when testing began.

Post-dissolution SEM micrographs of the pure UO_2 after the 25°C testing, Figure 9 C and D, showed smooth samples with no noticeable surface reactions beyond smoothing around the edges. This is consistent with the lower NDR and CF-U in comparison to the 75°C sample.

The post-dissolution micrographs of the pure UO_2 in the 75°C, Figure 9 E and F, showed apparent preferential grain boundary dissolution. This damage morphology was very pronounced in comparison to the pre-dissolution testing micrograph where the grain structure was not evident in the SEM micrographs. At 25ºC some faint grain structures could be seen but not as pronounced as the 75 ºC sample. From Figure 9F, it is clear that the average grain size of these samples is much smaller than typical fuels made by a fuel vendor which average 8 µm to 15 µm. The smaller grain size is another reason for the higher surface area relative to Casella et al. [3].

Collected EDS results pre- and post-dissolution studies are presented in Appendix B and C.

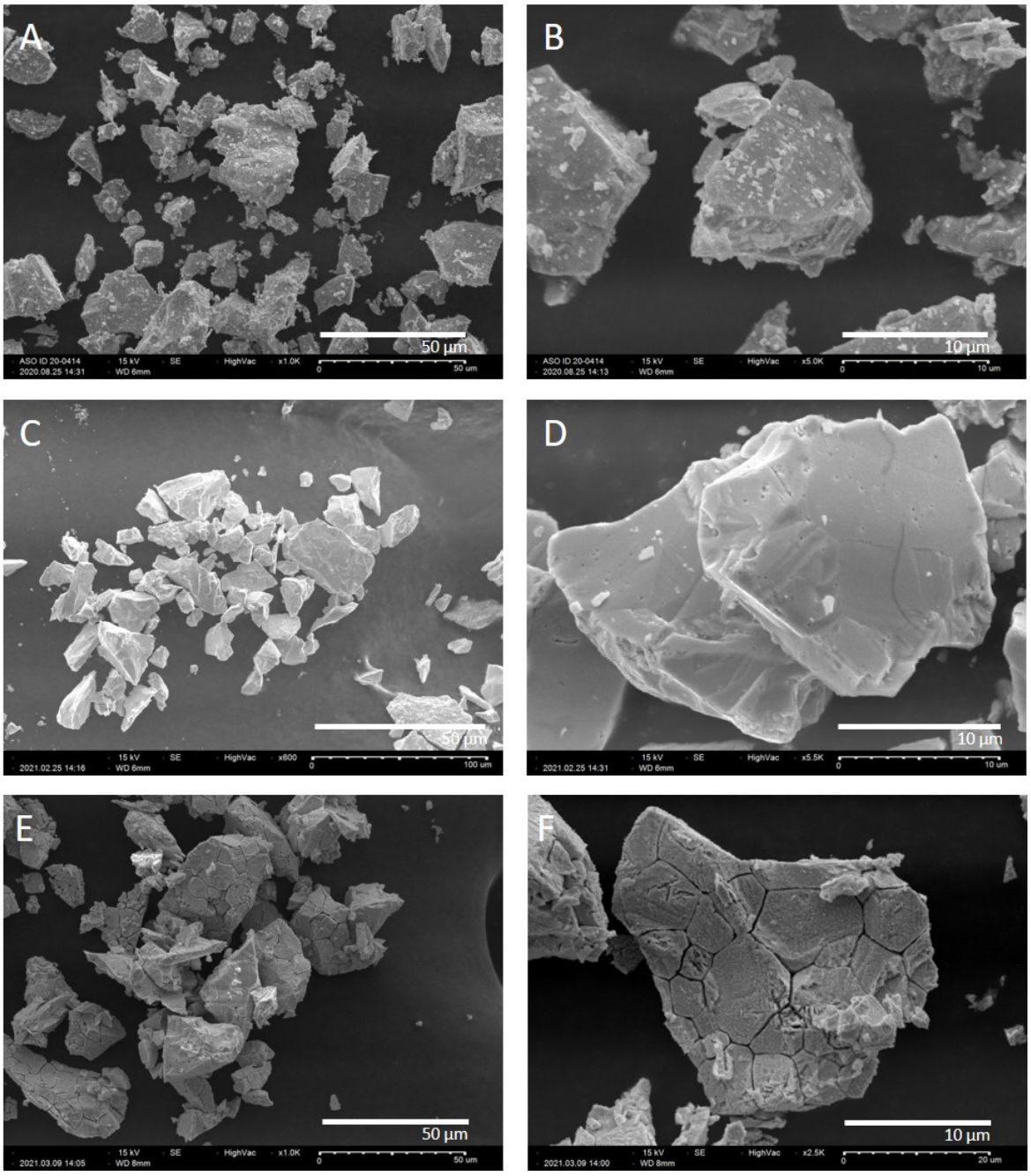

Figure 9. Pure UO_2 sample A) and B) pre-dissolution, C) and D) post-dissolution at 25°C, and E) and F) post-dissolution at 75°C.

3.2 Cerium Doping

3.2.1 Ce-doped UO_2 Powder SPFT Testing

The resulting NDR for the Ce-doped samples can be seen in Figure 10A for the 25 ºC tests and Figure 10B for the 75 ºC tests. All samples initially showed high NDRs as the fines remaining on the samples dissolved. In each graph the NDR for the pure UO_2 sample was included for comparison. At 25°C the 1% Ce-doped UO_2 and the pure UO_2 measured nearly identical NDR, Figure 10A, whereas the 5% Ce-doped sample measured a lower NDR. A similar trend was again observed at 75 ºC, Figure 10B, with the

pure UO_2 and the 1% Ce-doped UO_2 measuring similar NDR and the 5% Ce-doped UO_2 measuring the lowest NDR. Changing to less oxidizing conditions once again had a more pronounced effect in the 75ºC tests with a continual decrease in NDR. It was evident that increasing the Ce content slowed the dissolution of the simulated fuel sample.

The CF-U is shown in Figure 10C for the 25°C test and Figure 10D for the 75 ºC test. As expected, the CF-U showed the same trends as the NDR. Table 3 lists the average fraction release rate and the NDR from set time periods in the oxidizing and less oxidizing testing conditions. At 25ºC the 5% Ce doped sample had over 3× less U loss compared with the 1% Ce doped and the pure UO_2 and the CF-U for the 5% Ce sample was ~11× lower at 75 ºC. The rate of CF-U change at the onset of less oxidizing conditions decreased, and the rate of change in CF-U was generally lower in less oxidizing conditions than the oxidizing environment. The exception to this was the 1% Ce-doped sample at 25°C, which did not exhibit the same decrease in rate of CF-U. . Doping with 5% Ce suppressed the dissolution rate compared with UO_2, most evident in less oxidizing conditions.

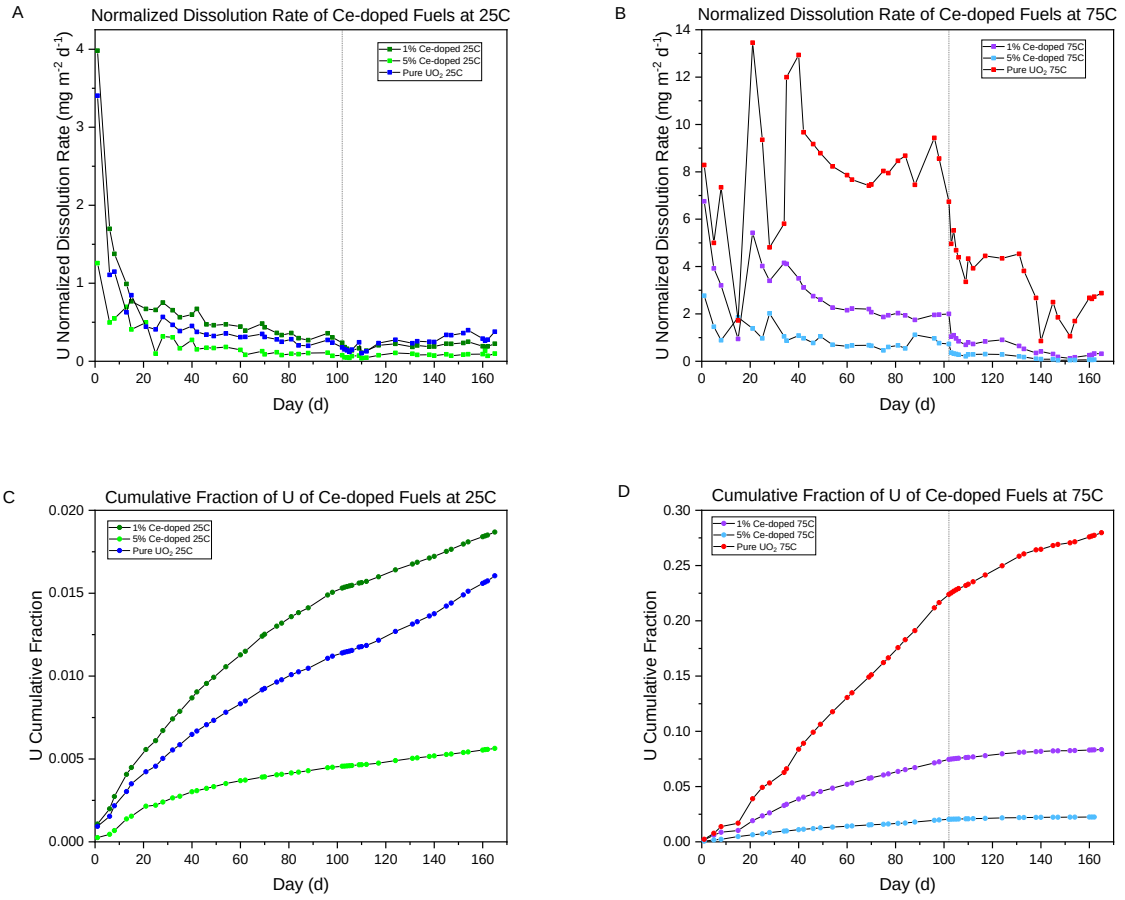

Figure 10. The Normalized Dissolution Rate (g m^{-2} d^{-1}) of Ce-doped UO_2 powder at A) 25°C and B) 75°C; the Cumulative Fraction of U of Ce-doped UO_2 powder at C) 25°C and D) 75°C.

Table 3. A comparison of the Average U Fractional Rate and the Average NDR of Ce-doped samples to the pure UO_2 control sample at set time periods during the oxidative and less oxidative testing.

Sample	Average U Fract. Rate (Day 75 – 102) during Oxidative Conditions (Std. Dev)	Average U Fract. Rate (Day 120-140) during Less Oxidative Conditions (Std. Dev)	Average NDR (Day 75 – 102) during Oxidative Conditions (Std. Dev)	Average NDR (Day 120-140) during Less Oxidative Conditions (Std. Dev)
Pure UO_2 25°C	6.52E-05 (1.11E-05)	8.99E-05 (1.46E-05)	2.38E-01 (4.06E-02)	3.28E-01 (5.33E-02)
1% Ce-Doped UO_2 25°C	8.52E-05 (1.26E-05)	5.91E-05 (6.50E-06)	3.16E-01 (4.67E-02) (	2.19E-01 (2.41E-02)
5% Ce-doped UO_2 25°C	1.88E-05 (3.35E-06)	1.69E-05 (1.83E-06)	9.29E-02 (1.66E-02)	8.34E-02 (9.06E-03)
Pure UO_2 75°C	2.24E-03 (2.25E-04)	4.86E-04 (2.02E-04)	8.16E+00 (8.22E-01)	1.77E+00 (7.36E-01)
1% Ce-doped UO_2 75°C	5.21E-04 (2.40E-05)	6.48E-05 (2.86E-05)	1.93E+00 (8.91E-02)	2.40E-01 (1.06E-01)
5% Ce-doped UO_2 75°C	1.48E-04 (4.41E-05)	1.29E-05 (3.93E-06)	7.31E-01 (2.18E-01)	6.40E-02 (4.41E-05)

3.2.2 Ce-doped UO_2 Powder Solids Analysis

Pre-test micrographs of the 1% Ce-doped, Figure 11A and Figure 11B, and 5% Ce-doped UO_2, Figure 11C and Figure 11D, again showed fines on the surface. Some porosity was observed on both Ce-doped samples prior to dissolution testing. It is unknown how the porosity was generated, but could be a result of the pressing and sintering process. However as seen in Figure 10A and B this porosity had little influence on the Ce-doped sample NDR compared to the pure UO_2. Upon closer inspection of the 5% Ce-doped sample, Figure 11D, increased magnification shows clear grain boundaries and pores within the sample on the order of 2 µm, which is atypical for sintered pellets.

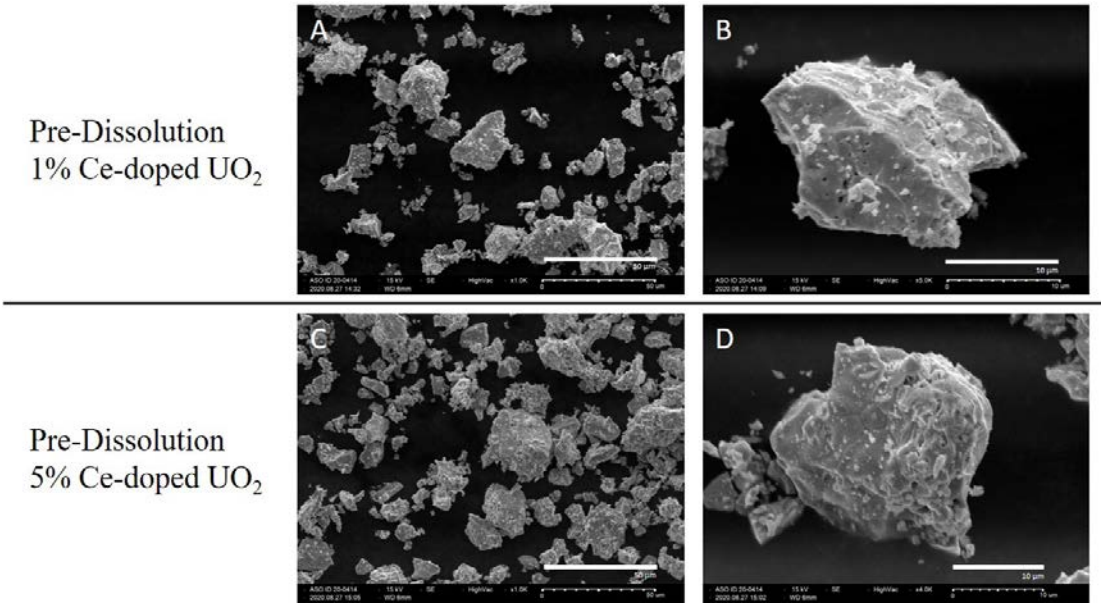

Figure 11. A) and B) 1% Ce-doped UO_2 pre-dissolution; C) and D) 5% Ce-doped UO_2 pre-dissolution.

In the post-dissolution micrographs of the 1% Ce-doped UO_2 at 25°C, the porosity of the sample was more noticeable and distinct than in the pre-dissolution images, Figure 12A and B. As well, there are grain boundaries that were visible at the higher magnification. The post-dissolution micrographs of the 5% Ce-doped UO_2 at 25°C, specifically in Figure 12D, shows porosity and dissolution of the sample compared to the pre-dissolution micrograph. At the higher magnifications the grain boundaries are also more evident compared to the lower magnification sample.

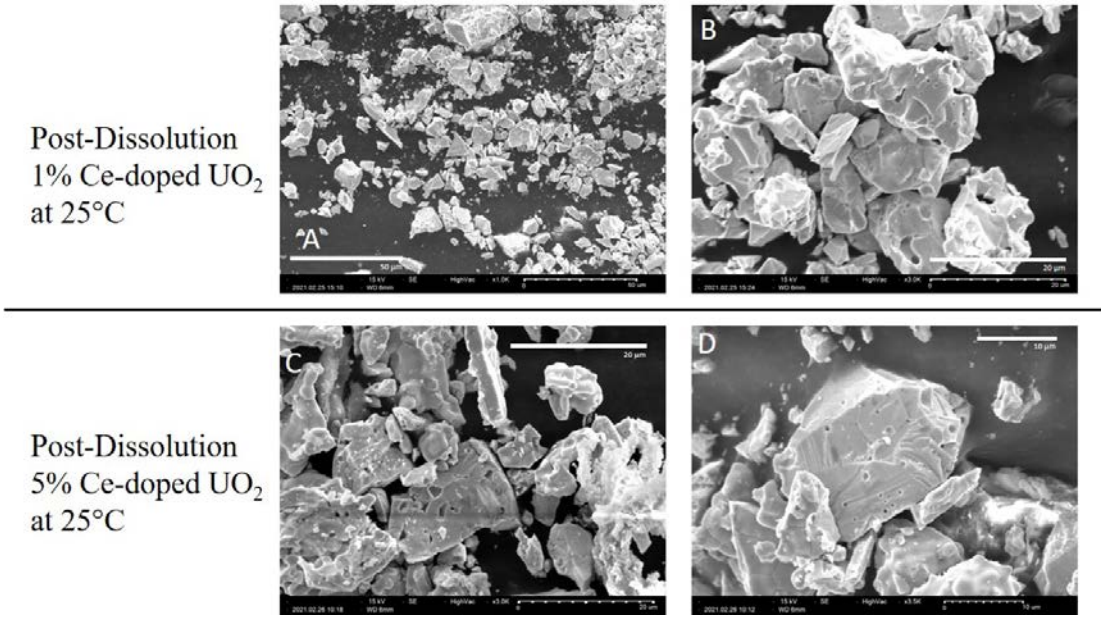

Figure 12. Post-dissolution micrographs of A) and B) 1% Ce-doped UO_2 and C) and D) 5% Ce-doped UO_2 at 25°C.

Post-dissolution images of the 1% and 5% Ce-doped UO_2 tested at 75°C, Figure 13, shows the same trends from the 25°C samples to a higher degree. The porosity of the samples is evident on both the 1%

and 5% Ce-doped samples. The post-dissolution 5% Ce-doped sample, Figure 13C and D, also shows rounded edges on the powder. Visually, the morphology of the 5% Ce-doped samples at 75°C was the most affected with the rounded sample and increased pore sizes. The grain boundary attack observed on the pure UO_2 sample was not as clearly observed on the Ce-doped samples.

Collected EDS results pre- and post-dissolution studies are presented in Appendix B and C.

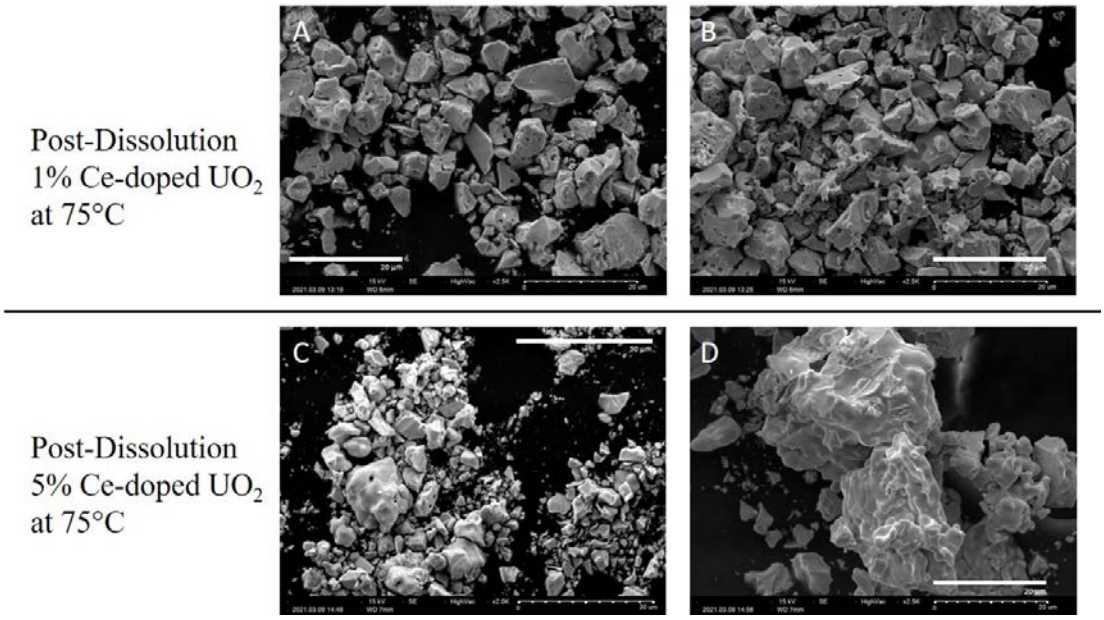

Figure 13. Post-dissolution micrographs of A) and B) 1% Ce-doped UO_2 and C) and D) 5% Ce-doped UO_2 at 75°C.

3.3 Neodymium Doping

3.3.1 Nd-doped UO_2 SPFT Testing

The NDR for the Nd-doped samples is seen in Figure 14A for the 25°C tests and in Figure 14B for the 75°C tests. The pure UO_2 sample result was included for comparison. The NDR of all samples at both temperatures was high initially as the remaining fines on the samples dissolved. The NDR of the 1% Nd-doped fuel and the pure UO_2 in the 25°C testing, Figure 14A, mirrored each other well for the remainder of the test, including when the sample was converted to less oxidizing conditions. For the duration of oxidative testing, the NDR showed a steady decrease in both the 1% and 5% Nd-doped samples, Figure 14A. Once the less oxidizing environment was simulated, the samples fluctuated with no clear trend. At the lower temperature of 25°C the higher dopant concentration was more effective in preventing dissolution. In the 75°C testing, Figure 14B, the 5% Nd-doped fuel at 75°C was not as effective in preventing dissolution in the 1% Nd-doped fuel. The 5% Nd-doped samples had higher fluctuations and no clear trend throughout testing, in both the oxidative and less oxidizing environment. Despite these fluctuations, the higher dopant concentration showed clear suppression of the dissolution of the samples in comparison to the pure UO_2.

The CF-U is shown in Figure 14C for the 25°C test, and in Figure 14D for the 75°C test. The Nd-containing sample at 25°C showed a higher fraction of U dissolved than the pure UO_2 until day 150. Results reflected trends observed in the NDR of the samples. Table 4 shows the average U fractional rate and the NDR at set time periods in the oxidative and less oxidative testing. The presence of Nd suppressed the dilution rate compared with UO_2, more so in less oxidizing conditions and at higher temperature.

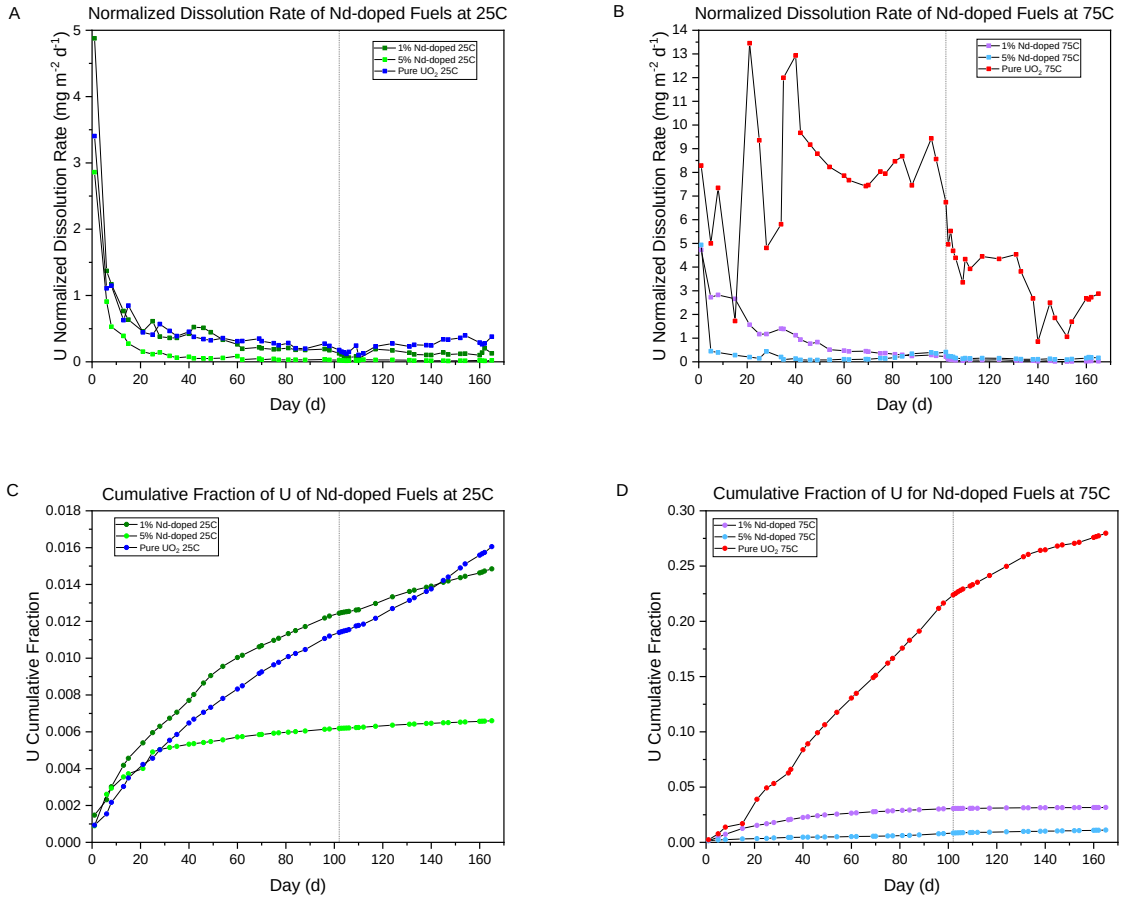

Figure 14. The Normalized Dissolution Rate (g m^{-2} d^{-1}) of Nd-doped UO_2 powder at A) 25°C and B) 75°C; the Cumulative Fraction of U of Nd-doped UO_2 powder at C) 25°C and D) 75°C.

Table 4. A comparison of the Average U Fractional Rate and the Average NDR of Nd-doped samples to the pure UO_2 control sample at set time periods during the oxidative and less oxidative testing.

Sample	Average U Fract. Rate (Day 75 – 102) during Oxidative Conditions (Std. Dev)	Average U Fract. Rate (Day 120-140) during Less Oxidative Conditions (Std. Dev)	Average NDR (Day 75 – 102) during Oxidative Conditions (Std. Dev)	Average NDR (Day 120-140) during Less Oxidative Conditions (Std. Dev)
Pure UO_2 25°C	6.52E-05 (1.11E-05)	8.99E-05 (1.46E-05)	2.38E-01 (4.06E-02)	3.28E-01 (5.33E-02)
1% Nd-Doped UO_2 25°C	5.46E-05 (7.17E-06)	3.52E-05 (4.53E-06)	1.80E-01 (2.37E-02)	1.16E-01 (1.49E-02)
5% Nd-doped UO_2 25°C	9.86E-06 (1.84E-06)	5.14E-06 (7.96E-07)	3.15E-02 (5.85E-03)	1.64E-02 (2.54E-03)
Pure UO_2 75°C	2.24E-03 (2.25E-04)	4.86E-04 (2.02E-04)	8.16E+00 (8.22E-01)	1.77E+00 (7.36E-01)

Sample	Average U Fract. Rate (Day 75 – 102) during Oxidative Conditions (Std. Dev)	Average U Fract. Rate (Day 120-140) during Less Oxidative Conditions (Std. Dev)	Average NDR (Day 75 – 102) during Oxidative Conditions (Std. Dev)	Average NDR (Day 120-140) during Less Oxidative Conditions (Std. Dev)
1% Nd-doped UO_2 75°C	8.87E-05 (1.57E-05)	6.45E-06 (3.32E-06)	2.93E-01 (5.18E-02)	2.13E-02 (1.10E-02)
5% Nd-doped UO_2 75°C	8.62E-05 (3.53E-05)	3.58E-05 (7.28E-06)	2.75E-01 (1.13E-01)	1.14E-01 (2.32E-02)

3.3.2 Nd-doped UO_2 Powder Solid Analysis

Pre-test micrographs of the 1% Nd-doped UO_2 powder, Figure 15A and B, and 5% Nd-doped UO_2 powder, Figure 15C and D, shows small particulate and fines on the sample surface. There was no obvious porosity of the sample, but the fines could obscure some of the surface features.

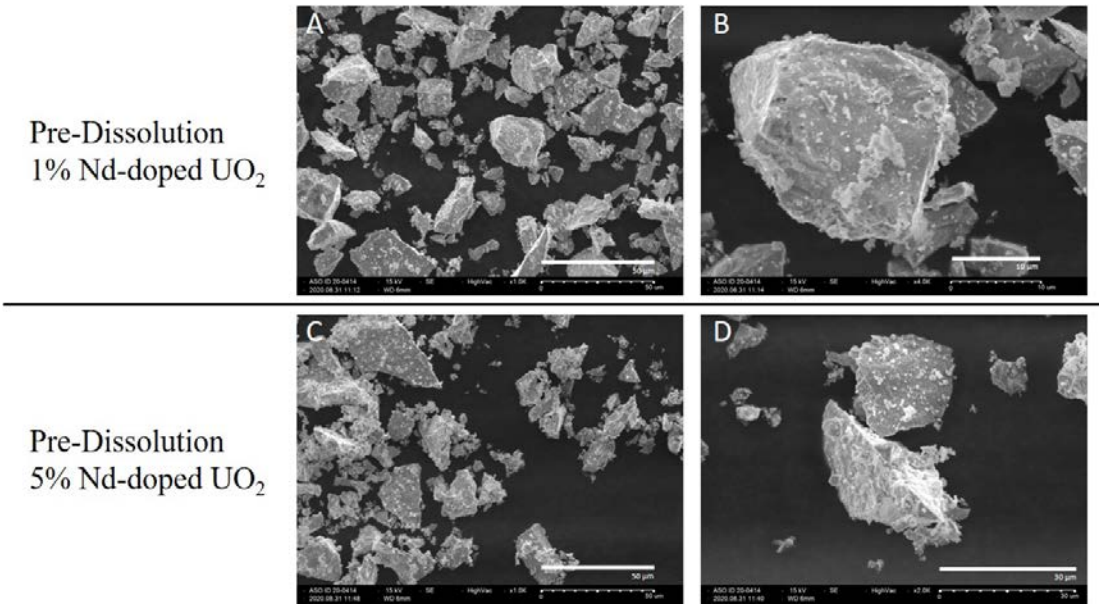

Figure 15. A) and B) 1% Nd-doped UO_2 pre-dissolution; C) and D) 5% Nd-doped UO_2 pre-dissolution.

Post-dissolution images of the 1% and 5% Nd-doped sample at 25°C showed a dramatic reduction in fines in the sample, Figure 16A through D, which was expected. In the 1% Nd-doped UO_2, Figure 16A and B, some of the grain boundaries became more apparent, showing the beginning of preferential grain boundary dissolution. However, the 5% Nd-doped sample, Figure 16C and D, showed obvious changes to the surface of the sample. While the fines may have been obscuring the pores on the surface the size of the pore has likely increased from the dissolution, and the grain boundary is clearly attacked as observed in the center of Figure 16D. There was some agglomeration of material in the 5% Nd-doped sample, but it cannot be confirmed that this is not a consequence of sample preparation.

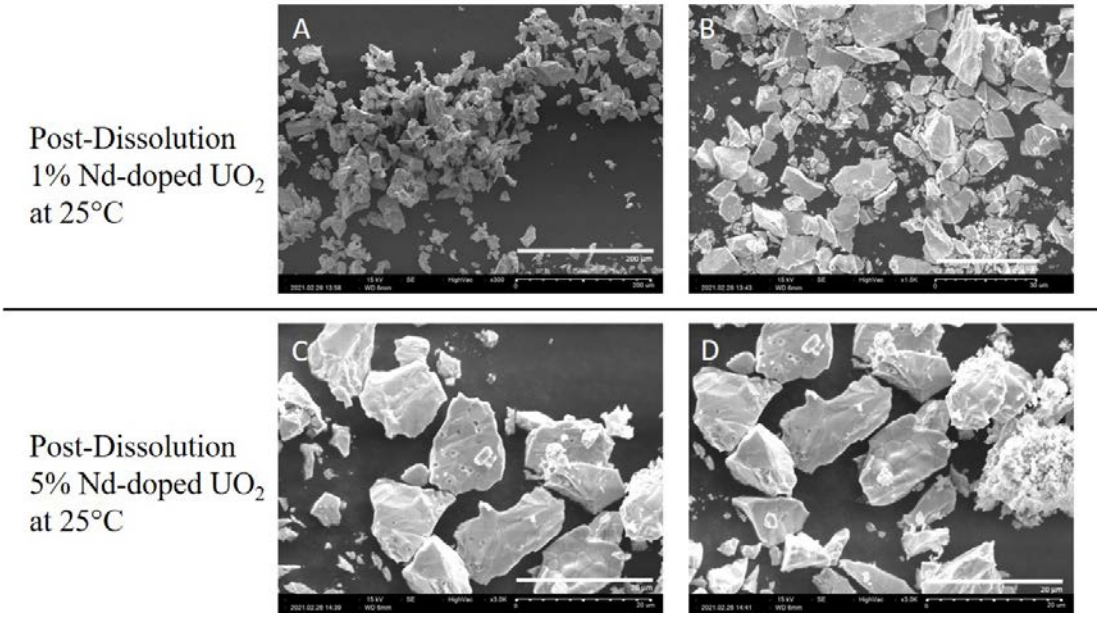

Figure 16. Post-dissolution micrographs of A) and B) 1% Nd-doped UO_2 and C) and D) 5% Nd-doped UO_2 at 25°C.

At the higher temperature testing of 75°C, post-dissolution micrographs, Figure 17, of the 1% and 5% Nd-doped UO_2 samples show similar results to the 25°C tests. The grain boundaries on the sample became apparent as well as some of the surface pores on the pieces of sample. However, despite the grains more obvious appearance, this was not as clear as the 5% Nd-doped UO_2 sample at 25°C. Fines and small fragments are evident in the post-dissolution images, particularly in Figure 17C and D, but this may also stem from the sample preparation method.

Collected EDS results pre- and post-dissolution studies are presented in Appendix B and C.

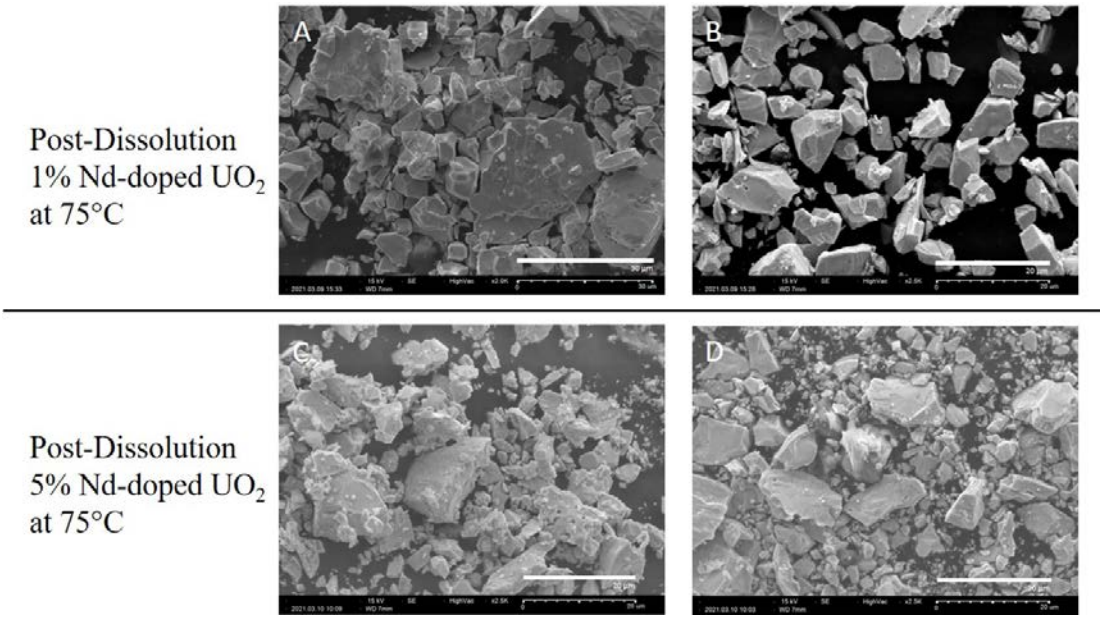

Figure 17. Post-dissolution micrographs of A) and B) 1% Nd-doped UO_2 and C) and D) 5% Nd-doped UO_2 at 75°C.

3.4 Ytterbium Doping

3.4.1 Yb-doped UO_2 SPFT Testing

The NDR for the Yb-doped samples can be seen in Figure 18A for the 25°C tests and Figure 18B for the 75°C tests. As observed previously, all samples showed initially high NDRs due to the fast dissolution of remaining fines. The pure UO_2 has been included on the graphs for comparison purposes.

The NDR of the Yb-doped samples at 25°C all performed relatively similar in the testing, Figure 18A. Following the fast dissolution of the fines, the slope of the NDR decreased and remained on a steady negative slope until the commencement of the reductive environment at day 102. In the reductive environment, while the pure UO_2 began an upwards trend, the two doped samples decreased steadily, with a few fluctuations. Conversely, the elevated temperature samples at 75°C, Figure 18B, did not reflect the trends of the pure UO_2 samples in that they decreased through the duration of most of the experiment, while the pure UO_2 showed more of a plateau. The addition of the Yb dopant showed clear dissolution resistance at the higher temperature tests, but had little effect on the reduction of dissolution in the 25°C testing.

The CF-U is shown in Figure 18C for the 25°C test and Figure 18D for the 75°C test. The CF-U shows the same trends as observed in the NDR graphs. Table 5 illustrates average fractional U release rate and the NDR at set time periods in the oxidative and less oxidative test conditions. Doping with Yb suppressed the dissolution rate compared with UO_2, more so in less oxidizing conditions.

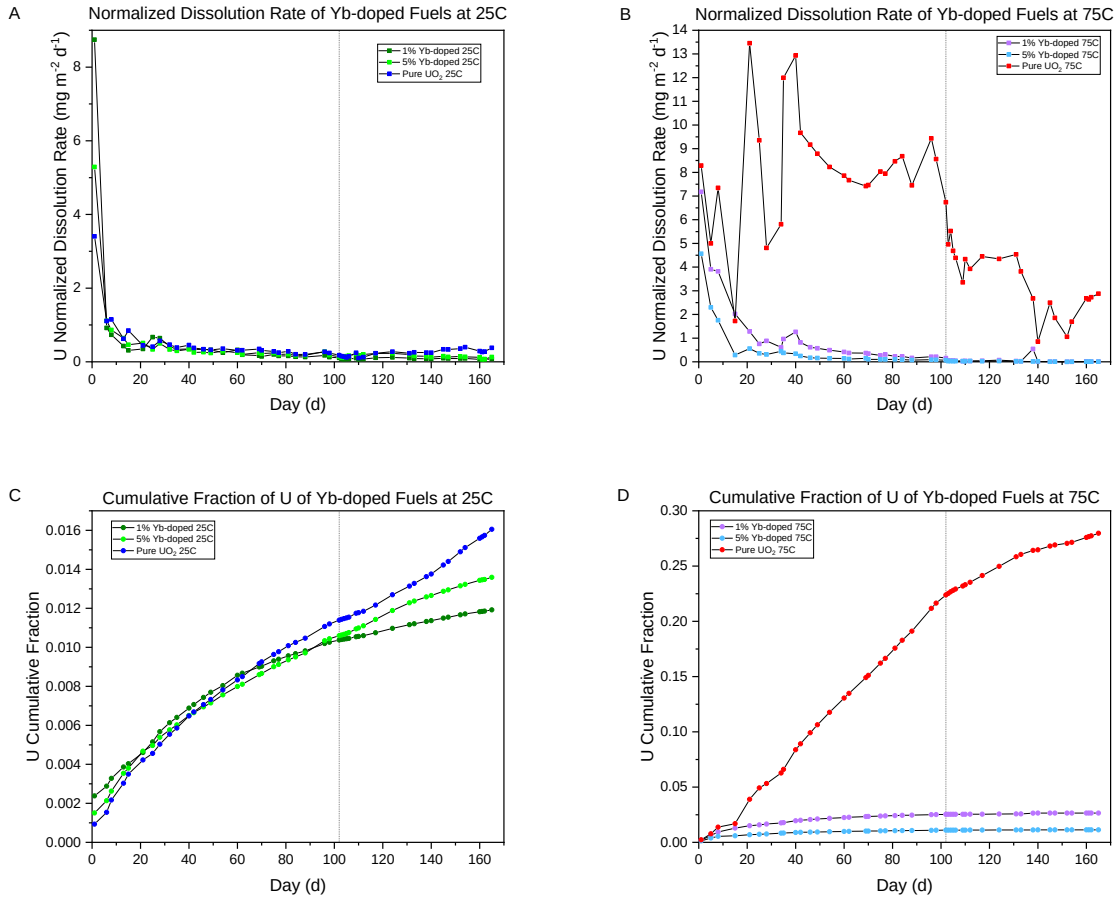

Figure 18. The Normalized Dissolution Rate (g m^{-2} d^{-1}) of Yb-doped UO_2 powder at A) 25°C and B) 75°C; the Cumulative Fraction of U of Yb-doped UO_2 powder at C) 25°C and D) 75°C.

Table 5. A comparison of the Average U Fractional Rate and the Average NDR of Yb-doped samples to the pure UO_2 control sample at set time periods during the oxidative and less oxidative testing.

Sample	Average U Fract. Rate (Day 75 – 102) during Oxidative Conditions (Std. Dev)	Average U Fract. Rate (Day 120-140) during Less Oxidative Conditions (Std. Dev)	Average NDR (Day 75 – 102) during Oxidative Conditions (Std. Dev)	Average NDR (Day 120-140) during Less Oxidative Conditions (Std. Dev)
Pure UO_2 25°C	6.52E-05 (1.11E-05)	8.99E-05 (1.46E-05)	2.38E-01 (4.06E-02)	3.28E-01 (5.33E-02)
1% Yb-Doped UO_2 25°C	4.06E-05 (7.91E-06)	2.32E-05 (2.79E-06)	1.49E-01 (2.91E-02)	8.51E-02 (1.02E-02)
5% Yb-doped UO_2 25°C	5.70E-05 (1.21E-05)	3.84E-05 (3.45E-06)	2.00E-01 (4.26E-02)	1.35E-01 (1.21E-02)
Pure UO_2 75°C	2.24E-03 (2.25E-04)	4.86E-04 (2.02E-04)	8.16E+00 (8.22E-01)	1.77E+00 (7.36E-01)

Sample	Average U Fract. Rate (Day 75 – 102) during Oxidative Conditions (Std. Dev)	Average U Fract. Rate (Day 120-140) during Less Oxidative Conditions (Std. Dev)	Average NDR (Day 75 – 102) during Oxidative Conditions (Std. Dev)	Average NDR (Day 120-140) during Less Oxidative Conditions (Std. Dev)
1% Yb-doped UO_2 75°C	6.04E-05 (1.41E-05)	1.45E-06 (1.54E-06)	2.22E-01 (5.19E-02)	5.33E-03 (5.66E-03)
5% Yb-doped UO_2 75°C	2.49E-05 (3.75E-06)	1.76E-06 (1.39E-06)	8.77E-02 (1.32E-02)	6.18E-03 (4.87E-03)

3.4.2 Yb-doped UO_2 Powder Solids Analysis

Micrographs of the 1% Yb-doped samples, Figure 19A and B, and the 5% Yb-doped samples, Figure 19C and D. Grain size and pores were not clearly visible on the pre-dissolution samples due to the fines on the surface. There were no distinct differences between the 1% and the 5% Yb-doped sample.

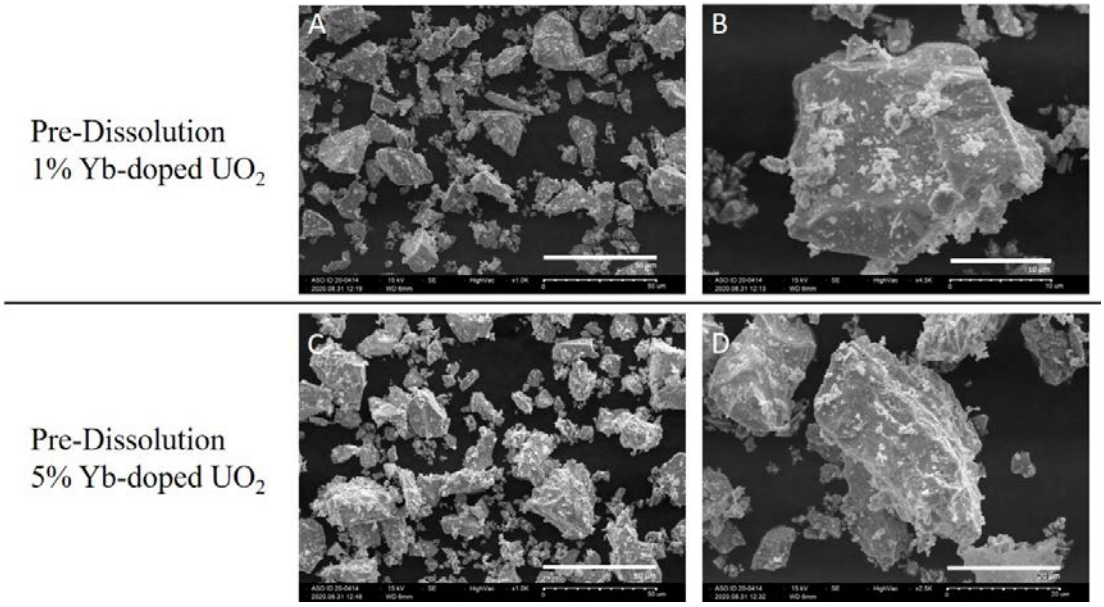

Figure 19. A) and B) 1% Yb-doped UO_2 pre-dissolution; C) and D) 5% Yb-doped UO_2 pre-dissolution.

In the post-dissolution micrographs of the 25°C samples, Figure 20, the removal of the fines shows the surface of the sample clearly, Figure 21. Some pores are evident on the surface, as well as the definition of grains on the surface of the powder particles. However, the sample did not show any significant dissolution attack.

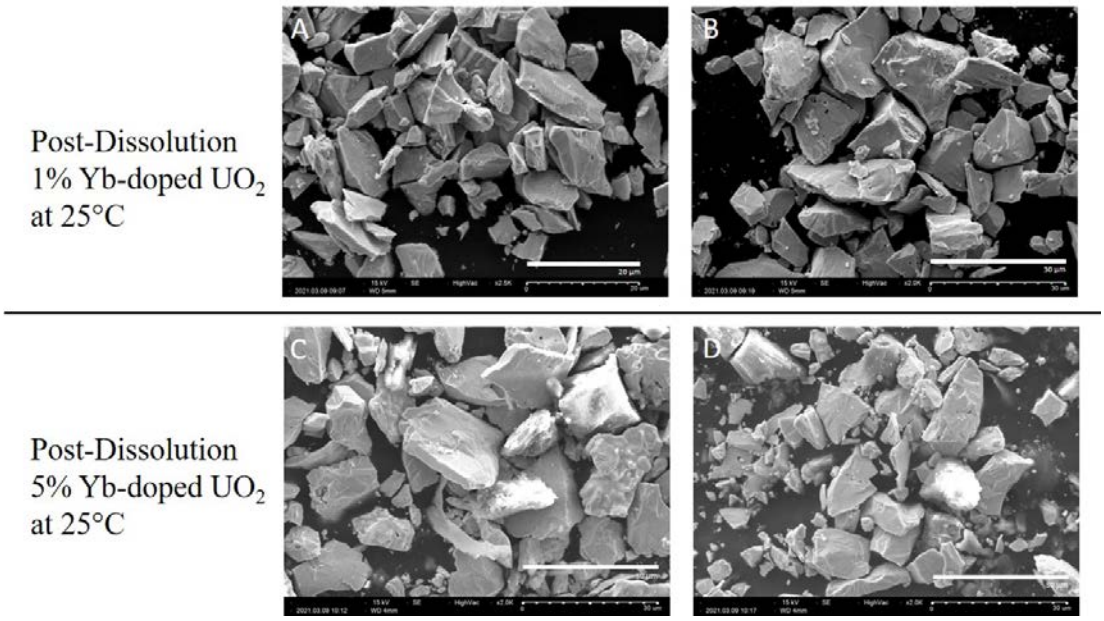

Figure 20. Post-dissolution micrographs of A) and B) 1% Yb-doped UO_2 and C) and D) 5% Yb-doped UO_2 at 25°C.

The elevated temperature samples showed far more surface alterations than the 25 ºC samples in both the 1% and 5% Yb-doped samples, Figure 21. In the 1% Yb-doped samples, Figure 21A and B, large pores are apparent on the surface of the powders, and the grain boundaries are slightly visible on some of the samples. The 5% Yb-doped samples at 75°C, Figure 21C and D, did not show visible pores, but clear grain boundary edges indicating dissolution at these interfaces. The grain boundary attack was not as clear evident as in the UO_2 sample (Figure 9F), but was more evident than on the other Yb-doped samples.

Collected EDS results pre- and post-dissolution studies are presented in Appendix B and C.

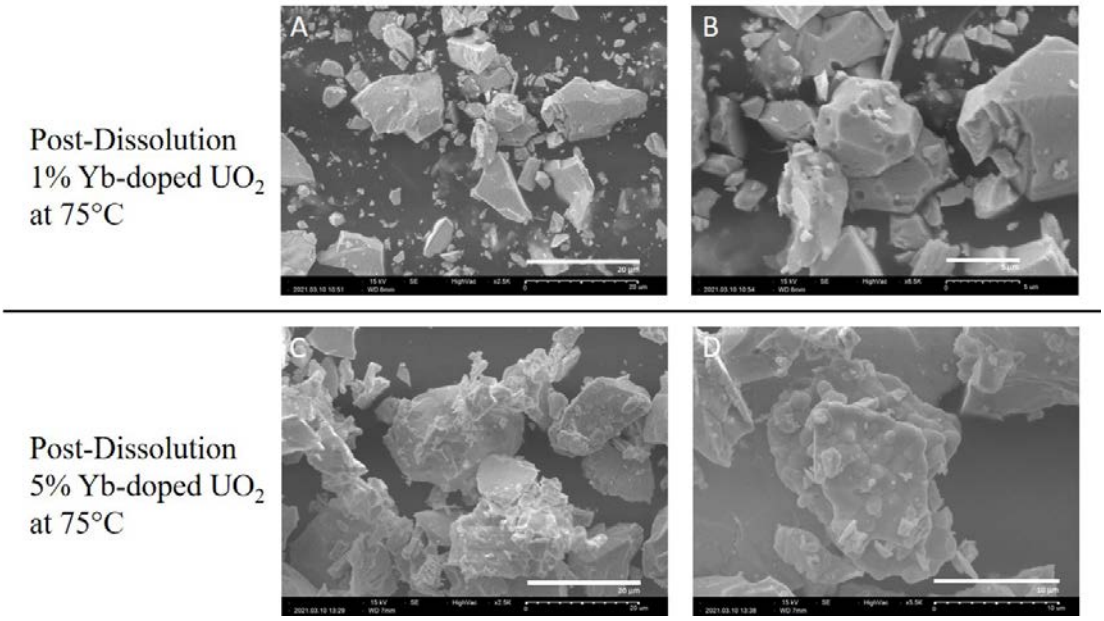

Figure 21. Post-dissolution micrographs of A) and B) 1% Yb-doped UO_2 and C) and D) 5% Yb-doped UO_2 at 75°C.

3.5 Ce-Doped UO_2 Fragment SPFT Testing

Fragment tests had very little measurable release due to the low surface area, however they give a valuable indication of bulk sample dissolution behavior. Resulting NDRs for the Ce-doped UO_2 fragments differed greatly for the samples at 25°C, Figure 22A, and the 75°C samples, Figure 22B. Dissolution of the fragment pieces at 25°C was very slow, and often any U in the sample collected was below detection limit, thus little to no sample accumulation was accounted for. This contributed to a very slow climb in CF-U, and sporadic jumps when U was detectable in the sample. It is important to note that this does not mean that no U was dissolved, but the amount in solution was too small to measure. The measured U content in samples in the 5% Ce-doped fragments run at 75°C was significantly higher. The CF-U in turn grew steadily during oxidative conditions. Following the sparge gas conversion to reductive conditions at 102 days, there were fluctuations until approximately day 103, where the NDR remained low overall.

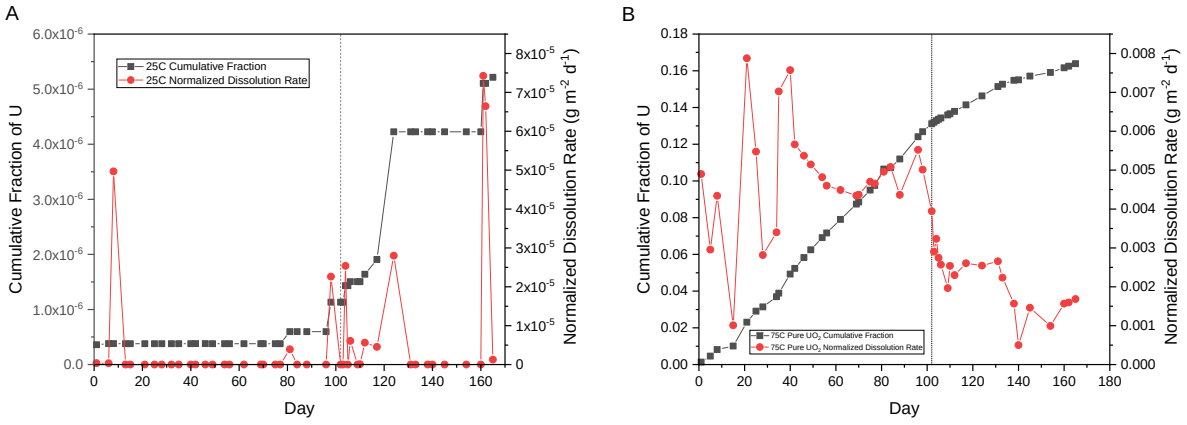

Figure 22. The Cumulative Fraction of U and the Normalized Dissolution Rate (g m^{-2} d^{-1}) of A) 5% Ce-doped UO_2 fragments at 25°C and B) 5% Ce-doped UO_2 fragments at 75°C.

A SEM image of the fragment samples was not taken prior to dissolution analysis due to the limited mass of sample available for testing. Figure 11C and D shows the powdered sample pre-dissolution which can be used as an indicator of what the fragment may have looked like. The grains are clearly visible in the pre-dissolution sample, with smaller fines scattered throughout the image. It is likely that fines and small fragments remained on the sample.

Post-dissolution imaging of the fragment following 25°C testing, Figure 23A, showed a smooth surface with clear grain boundaries. There is clear porosity, similar to that seen in the pre-dissolution samples, however post-dissolution the pores observed are larger in size.

The post-dissolution SEM imaging of the 5% Ce-doped fragments, Figure 23B, showed a very smooth surface with clear grain boundaries. In contrast to the 5% Ce-doped sample at 25°C, the surface showed a smooth appearance and dissolution at grain boundaries.

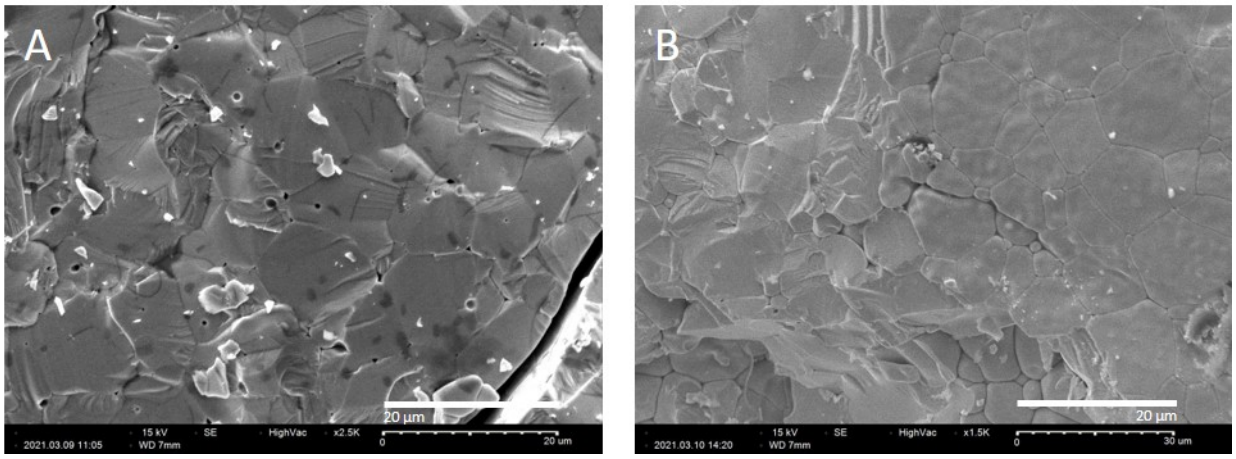

Figure 23. 5% Ce-doped fragments A) post-dissolution after 25°C testing and B) 75°C testing.

A comparison of the CF-U for the 25°C and the 75°C samples shows the dramatic difference in dissolution observed between the two, Figure 24. When compared to the dissolution of the powder samples, the fragment dissolution is much lower than all powder dissolution samples, with no effect of temperature. It is clear the dissolution in the fragments is different than that of the powders, and any comparisons that can be made are very limited. This is an agreement with previous studies that have shown that the dissolution of a pure UO_2 pellet or fragment is markedly reduced in comparison to that of a pure UO_2 powder [10, 42].

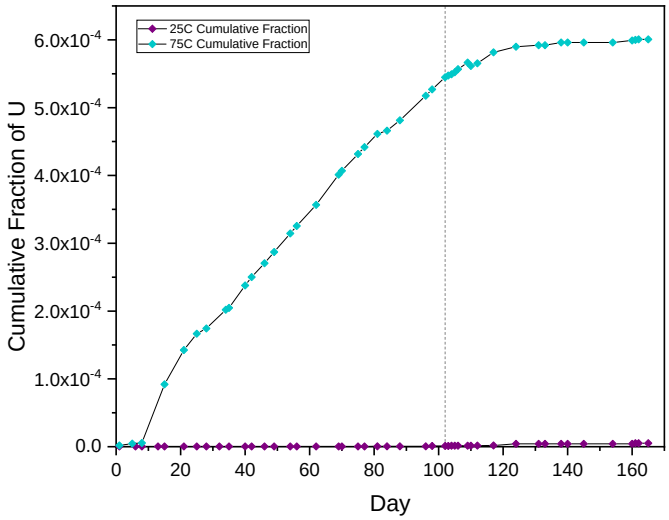

Figure 24. A comparison of the Cumulative Fraction of U for 5% Ce-doped UO_2 fragments at 25°C and 75°C.

This page is intentionally left blank.

4. DISCUSSION

4.1 Doping General Trends

The CF-U for each sample was measured to compare the temperature effects and the dopant effects. Generally, those samples with higher dopant content suppressed dissolution and reduced the NDR, most pronounced in higher temperature tests. The addition of 1% Ce dopant had less direct impact on the dissolution, however 5% Ce doping decreased the dissolution rate. The presence of Nd at 5% decreased the dissolution rate at both test temperatures, while the 1% Nd doped sample had a lower dissolution in the 75ºC test. The presence of Yb led to decreased dissolution rates with increased Yb content at both test temperatures.

Previous studies have indicated that when UO_2 is doped with trivalent cations, the charge compensation mechanism that occurs within the structure are not element dependent [43]. The valence state of the dopant instead impacts the charge compensation that occurs within the UO_2 matrix. Redox studies have shown that doping generally decreases the redox activity of the UO_2 [10]. Oxidation of Ce-doped UO_2 samples occurs through two pathways, depending on the dopant concentration [33]. Previous research observed that oxidation of the UO_2 was delayed with the Ce dopant addition [33]. A similar effect may be observed in this work. The results in this study support these hypotheses, however the effect of trivalent cation dopants may not be universal at different doping level.

4.1.1 Oxidative Testing Comparison

Similar trends overall were observed in oxidizing conditions between the samples with the various dopants. Generally, the addition of dopant did suppress the NDR in comparison to the pure UO_2 sample in oxidative conditions. The exception to this is in the case of the 1% Ce-doped UO_2 sample which had a higher average NDR than the pure UO_2. In the oxidative conditions the lowest U fractional release rates were measured for the 5% Ce and 5% Nd samples at 25ºC and the 1% Yb and 5% Yb samples at 75 ºC. In the 25°C tests, the higher dopant concentration reduced the NDR by as much as 7× the pure UO_2 sample. For the 75°C samples this reduction in NDR was 12× (5% Ce-doped) to 93× (5% Yb-doped) depending on the identity of the dopant. At the higher temperature oxidative tests, the higher dopant content clearly was more effective in suppressing dissolution of the sample. As well, Yb was the most effective in suppression, while Ce showed the least effectivity. Table 6 (25 ºC tests) and Table 7 (75 ºC tests) compare the NDR in the oxidative conditions for all samples ranking them from most corrosion resistant (lowest NDR) to least durable (highest NDR).

Table 6. A Comparison of the NDR of U from 25°C samples in the test matrix, in order of increasing corrosion resistance at the conclusion of the oxidative testing.

Sample	Average NDR (75 – 102 Days)
5% Nd	0.0315
5% Ce	0.0929
1% Yb	0.1493
1% Nd	0.1802
5% Yb	0.2003
Pure UO_2	0.2380
1% Ce	0.3159

Table 7. A Comparison of the NDR of U from 75°C samples in the test matrix, in order of increasing corrosion resistance at the conclusion of the oxidative testing.

Sample	Average NDR (75 – 102 days)
5% Yb	0.0877
1% Yb	0.2218
5% Nd	0.2749
1% Nd	0.2926
5% Ce	0.7309
1% Ce	1.9320
Pure UO_2	8.1631

4.1.2 Reductive Testing Comparison

Visually on the NDR and CF-U vs time figures it was observed that the conversion from oxidation conditions (higher O_2 ppm) to less oxidizing conditions (lower O_2 ppm) suppressed the NDR and resulting CF-U, an effect most pronounced in the 75 ºC tests.

The results of the CF-U and NDR from the reductive testing showed minimal similarities to the results of the oxidative conditions. Table 8 and Table 9 presents the NDR from the lowest release to the highest release in the reductive conditions at 25 ºC and 70 ºC respectively. The NDR presented in the tables is the NDR average measured only during the less oxidizing condition period. All dopant concentrations had a clear influence in suppressing the dissolution of the samples compared to pure UO_2. It should be noted that longer-term tests in less oxidizing conditions would provide better comparisons between the samples due to the overall low dissolution rate.

Table 8. A Comparison of the average NDR of U from 25°C samples in the test matrix during less oxidizing conditions, in order of corrosion resistance.

Sample	Average NDR (120 – 140 days)
5% Nd	0.0164
5% Ce	0.0834
1% Yb	0.0851
1% Nd	0.1160
5% Yb	0.1351
1% Ce	0.2193
Pure UO_2	0.3278

Table 9. A Comparison of the average NDR of U from 75°C samples in the test matrix during less oxidizing conditions, in order of corrosion resistance.

Sample	Average NDR (120 – 140 days)
1% Yb	0.0053
5% Yb	0.0062
1% Nd	0.0213
5% Ce	0.0640
5% Nd	0.1143
1% Ce	0.2404
Pure UO_2	1.7725

4.1.3 Dopant Effect Summary

Ultimately, the presence of dopant reduced the dissolution of samples in comparison to the pure UO_2, In the oxidative testing, those samples with higher dopant concentration tended to provide higher dissolution resistance.

An experiment examining long-term testing in the less oxidizing conditions would be valuable to give better comparison to the oxidative testing. Furthermore, cycling between oxidizing and less oxidizing conditions, which has been shown to be possible here, would provide valuable further insight into the influence of less oxidizing conditions with varying fuel chemistry.

The effect of dopant concentration beyond 5 at% would be of interest to understand how the system changes with increasing dopant. The addition of more testing temperatures would assist data interpretation by allowing an Arrhenius relationship assessment and possibly determine an activation energy for the dissolution process.

Other samples of interest in the immediate future are Cr and/or Al doped fuels, as well as mixed oxide (MOX) fuels. Many European laboratories are studying these fuels in less oxidizing environments, and oxidative testing would be complimentary to these studies to fully understand the characteristics of the fuels. Combinations of dopants are also of interest to understand if the oxygen vacancies are similarly affected in the presence of multiple dopants.

4.2 Dissolution Mechanism and Redox Conditions

To gain insights into the dissolution mechanism of the fuel samples and resulting corrosion morphologies the fuel surfaces were examined by SEM following the tests. Some samples, in particular the pure UO_2 at 75°C, 5% Ce-doped UO_2 at 75°C, 5% Nd-doped UO_2 at 25°C, and the 5% Yb-doped UO_2 at 75°C, showed clear signs of preferential grain boundary dissolution with the boundaries becoming more prominent and easily observed in post-dissolution studies. This preferential grain boundary attack may be caused by heterogeneous chemistry at the boundaries compared to the fuel matrix making the boundaries more susceptible. Alternatively, it is possible that the higher concentration of dopants generated a more durable matrix. This preferential grain boundary attack is seen in both air oxidation and oxidative dissolution of spent fuel or doped-UO_2 whereas pure UO_2 exhibits a more uniform oxidation front starting at the sample surface.

A consequence of this behavior would be that less-soluble radionuclides which migrate to the grain boundaries could be preferentially released from the fuel. This process would need to be represented in a

predictive model. The other samples with lower dopant levels and lower test temperatures in general showed some increased porosity, but otherwise minimal effects on the surface of the sample.

Most pre-dissolution micrographs of powder samples showed that the small fines that were initially present on all samples were removed from the surface during testing. However, a select few (5% Ce-doped at 75°C, 1% and 5% Nd-doped at 25°C, and 5% Nd-doped at 75°C) exhibit small particulate or fines on the post-dissolution sample micrograph. This is attributed to the sample preparation for SEM, not the formation of precipitates or new fines. Some of the material needed to be crushed slightly after removal from the flowcell because it had agglomerated together during testing.

5. SUMMARY

This report was prepared to support the continuing effort to improve the FMDM for use in long-term modeling of SNF in a repository. SPFT testing was carried out on fuel samples doped with various levels of Ce, Yb and Nd in sequential oxidizing and less oxidizing conditions.

For Ce doping it was observed that increasing the Ce content to 5 at% of the sample slowed the dissolution of the simulated fuel sample. The exception to this was the 1% Ce doped sample at high temperature, which did not show as high resistance that the other samples did in comparison to the pure UO_2. With Nd doping the fuel dissolution showed clearly that the higher dopant content suppressed sample dissolution. The presence of Yb in the room temperature samples showed only slight suppression of dissolution in comparison to the pure UO_2 sample. However, at the high temperature, a clear trend of dissolution suppression with Yb doping was observed.

In general, upon switching from oxidizing to less oxidizing conditions the dissolution rate of the fuel samples decreased, an effect most pronounced at higher temperature. Investigation of the fuel samples after corrosion showed a preferential grain boundary dissolution on the following samples: pure UO_2 at 75°C, 5% Ce-doped UO_2 at 75°C, 5% Nd-doped UO_2 at 25°C, and the 5% Yb-doped UO_2 at 75°C. Other samples, such as 1% Ce-doped UO_2 at 25°C, 5% Ce-doped samples at 25°C and 75°C, 1% Yb-doped UO_2 at 75°C, 1% and 5% Yb-doped UO_2 at 25°C, showed increased pore sizes post-dissolution as well as some rounded edges. These results help further our understanding of the role of rare earth fission products controlling UO_2 dissolution in oxidizing and less oxidizing conditions.

Future work using the SPFT system includes dopant combinations to determine the effects of multiple species present, increased dopant content, and in particular, the study of simulated fuels containing Cr and/or Al, both combined and separate. Increasing the range of components, temperatures, and environments will help in further understanding the behavior of fuels in a variety of repository conditions. Modifications to the system will be made to better approach anoxic and reducing conditions as best as possible with the limitations on use of hydrogen as a sparge gas. The results of this work further our understanding of the role of dopants and redox conditions on SNF dissolution. The information will be critical moving forward to improving the FMDM.

This page is intentionally left blank.

6. REFERENCES

1. Christensen, H. and S. Sunder, *Current State of Knowledge of Water Radiolysis Effects on Spent Nuclear Fuel Corrosion.* Nuclear Technology, 2000. **131**(1): p. 102-123.
2. Pastina, B. and J.A. LaVerne, *Effect of Molecular Hydrogen on Hydrogen Peroxide in Water Radiolysis.* The Journal of Physical Chemistry A, 2001. **105**(40): p. 9316-9322.
3. Casella, A., B. Hanson, and W. Miller, *The effect of fuel chemistry on UO2 dissolution.* Journal of Nuclear Materials, 2016. **476**: p. 45-55.
4. Shoesmith, D.W., *Fuel corrosion processes under waste disposal conditions.* Journal of Nuclear Materials, 2000. **282**(1): p. 1-31.
5. Giménez, J., et al., *Oxidation and dissolution of UO2 in bicarbonate media: Implications for the spent nuclear fuel oxidative dissolution mechanism.* Journal of Nuclear Materials, 2005. **345**(2): p. 232-238.
6. Razdan, M. and D.W. Shoesmith, *The Electrochemical Reactivity of 6.0 wt% Gd-Doped UO2in Aqueous Carbonate/Bicarbonate Solutions.* Journal of The Electrochemical Society, 2014. **161**(4): p. H225-H234.
7. Jégou, C., et al., *Effect of external gamma irradiation on dissolution of the spent UO2 fuel matrix.* Journal of Nuclear Materials, 2005. **341**(1): p. 62-82.
8. Cunnane, J., *CSNF Waste Form Degradation: Summary Abstraction*. 2004, Yucca Mountain Project, Las Vegas, NV (United States). p. Medium: ED.
9. Swift, P.N. and E.J. Bonano, *Geological Disposal of Nuclear Waste in Tuff: Yucca Mountain (USA) [Geological Disposal in Tuff: Yucca Mountain]*. Elements, 2016: p. Medium: ED; Size: p. 263-268.
10. Pehrman, R., et al., *On the redox reactivity of doped UO2 pellets – Influence of dopants on the H2O2 decomposition mechanism.* Journal of Nuclear Materials, 2012. **430**(1): p. 6-11.
11. Jonsson, M., et al., *Radiation Induced Spent Nuclear Fuel Dissolution under Deep Repository Conditions.* Environmental Science & Technology, 2007. **41**(20): p. 7087-7093.
12. Stennett, M.C., et al., *Preparation, characterisation and dissolution of a CeO2 analogue for UO2 nuclear fuel.* Journal of Nuclear Materials, 2013. **432**(1): p. 182-188.
13. Odorowski, M., et al., *Effect of metallic iron on the oxidative dissolution of UO2 doped with a radioactive alpha emitter in synthetic Callovian-Oxfordian groundwater.* Geochimica et Cosmochimica Acta, 2017. **219**: p. 1-21.
14. Fanghänel, T., et al., *Reducing Uncertainties Affecting the Assessment of the Long-Term Corrosion Behavior of Spent Nuclear Fuel.* Inorganic Chemistry, 2013. **52**(7): p. 3491-3509.
15. Ewing, R.C., *Long-term storage of spent nuclear fuel.* Nature Materials, 2015. **14**(3): p. 252-257.
16. Nielsen, F., K. Lundahl, and M. Jonsson, *Simulations of H2O2 concentration profiles in the water surrounding spent nuclear fuel.* Journal of Nuclear Materials, 2008. **372**(1): p. 32-35.
17. Burns, P.C., R.C. Ewing, and A. Navrotsky, *Nuclear Fuel in a Reactor Accident.* Science, 2012. **335**(6073): p. 1184-1188.
18. Santos, B.G., J.J. Noël, and D.W. Shoesmith, *The effect of pH on the anodic dissolution of SIMFUEL (UO2).* Journal of Electroanalytical Chemistry, 2006. **586**(1): p. 1-11.
19. Hanson, B.D., *Examining the Conservatisms in Dissolution Rates of Commercial Spent Nuclear Fuel*. 2008: United States. p. 8.
20. Goldik, J.S., et al., *Surface electrochemistry of UO2 in dilute alkaline hydrogen peroxide solutions.* Electrochimica Acta, 2004. **49**(11): p. 1699-1709.
21. Eriksen, T.E., D.W. Shoesmith, and M. Jonsson, *Radiation induced dissolution of UO2 based nuclear fuel – A critical review of predictive modelling approaches.* Journal of Nuclear Materials, 2012. **420**(1): p. 409-423.
22. Hanson, B.D., et al., *Corrosion of commercial spent nuclear fuel. 1. Formation of studtite and metastudtite*. Radiochimica Acta, 2005. **93**(3): p. 159-168.

23. McNamara, B., et al., *Corrosion of commercial spent nuclear fuel 2 Radiochemical analyses of metastudtite and leachates.* Radiochimica Acta, 2005. **93**(3): p. 169-175.
24. Serrano-Purroy, D., et al., *Instant release fraction and matrix release of high burn-up UO2 spent nuclear fuel: Effect of high burn-up structure and leaching solution composition.* Journal of Nuclear Materials, 2012. **427**(1): p. 249-258.
25. Clarens, F., et al., *Formation of Studtite during the Oxidative Dissolution of UO2 by Hydrogen Peroxide: A SFM Study.* Environmental Science & Technology, 2004. **38**(24): p. 6656-6661.
26. Razdan, M. and D.W. Shoesmith, *Influence of Trivalent-Dopants on the Structural and Electrochemical Properties of Uranium Dioxide (UO2).* Journal of The Electrochemical Society, 2013. **161**(3): p. H105-H113.
27. Scheele, R.D., et al. *Effect of Gadolinium Doping on the Air Oxidation of Uranium Dioxide*. in *Scientific Basis for Nuclear Waste Management XXVIII*. 2004. Warrendale, Pennsylvania: Materials Research Society.
28. McEachern, R.J., et al., *Determination of the activation energy for the formation of U3O8 on UO2.* Journal of Nuclear Materials, 1997. **249**(1): p. 58-69.
29. McEachern, R.J., D.C. Doern, and D.D. Wood, *The effect of rare-earth fission products on the rate of U3O8 formation on UO2.* Journal of Nuclear Materials, 1998. **252**(1): p. 145-149.
30. Hanson, B.D., *The burnup dependence of light water reactor spent fuel oxidation*. 1998, ; Pacific Northwest National Lab., Richland, WA (United States). p. Medium: ED; Size: [200] p.
31. Scheele, R.D., B.D. Hanson, and A.M. Casella, *Effect of added gadolinium oxide on the thermal air oxidation of uranium dioxide.* Journal of Nuclear Materials, 2021. **552**: p. 153008.
32. Olds, T.A., et al., *Oxidation and anion lattice defect signatures of hypostoichiometric lanthanide-doped UO2*. Journal of Nuclear Materials, 2020. **530**: p. 151959.
33. Ha, Y.-K., et al., *Effect of Ce doping on UO2 structure and its oxidation behavior*. Journal of Nuclear Materials, 2016. **480**: p. 429-435.
34. Buck, E.C., et al., *Coupling the Mixed Potential and Radiolysis Models for Used Fuel Degradation*. 2013: United States.
35. Jerden, J.L., K. Frey, and W. Ebert, *A multiphase interfacial model for the dissolution of spent nuclear fuel.* Journal of Nuclear Materials, 2015. **462**: p. 135-146.
36. Mariner, P.E., et al. *High Fidelity Surrogate Modeling of Fuel Dissolution for Probabilistic Assessment of Repository Performance*. in *International High-Level Radioactive Waste Management*. 2019. Knoxville, TN.
37. Mennecart, T., et al., *Effect of alpha radiolysis on doped UO2 dissolution under reducing conditions*, in *Radiochimica Acta*. 2004. p. 611.
38. Röllin, S., K. Spahiu, and U.B. Eklund, *Determination of dissolution rates of spent fuel in carbonate solutions under different redox conditions with a flow-through experiment.* Journal of Nuclear Materials, 2001. **297**(3): p. 231-243.
39. Hanson, B.D., J.I. Friese, and C.Z. Soderquist, *Initial Results From Dissolution Testing of Spent Fuel Under Acidic Conditions.* MRS Proceedings, 2004. **824**: p. CC8.6.
40. Hanson, B.D. and R.B. Stout, *Reexamining the Dissolution of Spent Fuel: A Comparison of Different Methods for Calculating Rates.* MRS Proceedings, 2004. **824**: p. CC2.4.
41. Casella, A.J., *The Dissolution Rate of Unirradiated UO_2 Under Repository Conditions: the Influence of Fuel and Water Chemistry, Dissolved Oxygen, and Temperature*, in *Nuclear Engineering*. 2008, University of Missouri - Columbia.
42. Nilsson, S. and M. Jonsson, *H2O2 and radiation induced dissolution of UO2 and SIMFUEL pellets.* Journal of Nuclear Materials, 2011. **410**(1): p. 89-93.
43. Herrero, B., et al., *Charge compensation mechanisms in Nd-doped UO2 samples for stoichiometric and hypo-stoichiometric conditions: Lack of miscibility gap.* Journal of Nuclear Materials, 2020. **539**: p. 152276.

Appendix A

Table A-1. Incidents during testing.

Day	Affected Columns	Incident
4	A1 through A7	Columns not flowing well; stopped all columns to replace top frits. Stopped for 16 hrs total.
13	B1 through B8	Columns not flowing well or at all; turned off pumps and oven overnight and changed all top frits, and B8 bottom frit.
22	A1 through A8	Column flow rate decreased significantly; turned off all pumps and changed out top frits. Stopped for 30 minutes.
112	A4	Pump head was found to be disconnected from the piston and resulted in no pumping; flow was compromised. The top and bottom frits may have clogged with sample; top and bottom frits were removed and replaced. Pump was off for 27.5 hours.
165	B3	B3 pump was unplugged and had no flow for three days.

The amount of sample lost per frit after removal was quantified to determine the impact on the system. This was performed by placing the frit in 3 mL of 3 M HNO_3 to dissolve the sample within the frit. Following dissolution time, an aliquot was removed for KPA analysis to determine the mass of U lost from the total sample, Table A-2. The mass loss at each step was accounted for when calculating the NDR and Cumulative Fraction.

Table A-2. Calculated mass loss from frit clogging incidents.

Day	Frit Column ID	Mass Lost (mg)	Percent Total Mass Loaded (%)
4	A1 Top	1.035	1.06%
4	A2 Top	2.977	1.83%
4	A3 Top	2.645	1.62%
4	A4 Top	2.135	1.06%
4	A5 Top	3.837	1.87%
4	A6 Top	11.156	7.52%
4	A7 Top	17.190	9.23%
13	B1 Top	3.112	2.53%
13	B2 Top	1.179	0.57%
13	B3 Top	3.865	1.92%
13	B4 Top	4.842	2.36%
13	B5 Top	8.489	4.18%
13	B6 Top	3.063	2.08%

Day	Frit Column ID	Mass Lost (mg)	Percent Total Mass Loaded (%)
13	B7 Top	5.591	2.82%
13	B8 Bottom	0.006	0.00%
13	B8 Top	0.026	0.02%
22	A1 Top	0.213	0.22%
22	A2 Top	1.350	0.83%
22	A3 Top	0.001	0.00%
22	A4 Top	1.289	0.64%
22	A5 Top	2.995	1.46%
22	A6 Top	0.241	0.16%
22	A7 Top	0.574	0.31%
22	A8 Top	0.021	0.01%

Appendix B

The EDS results for the pre-dissolution samples are shown in Appendix B.

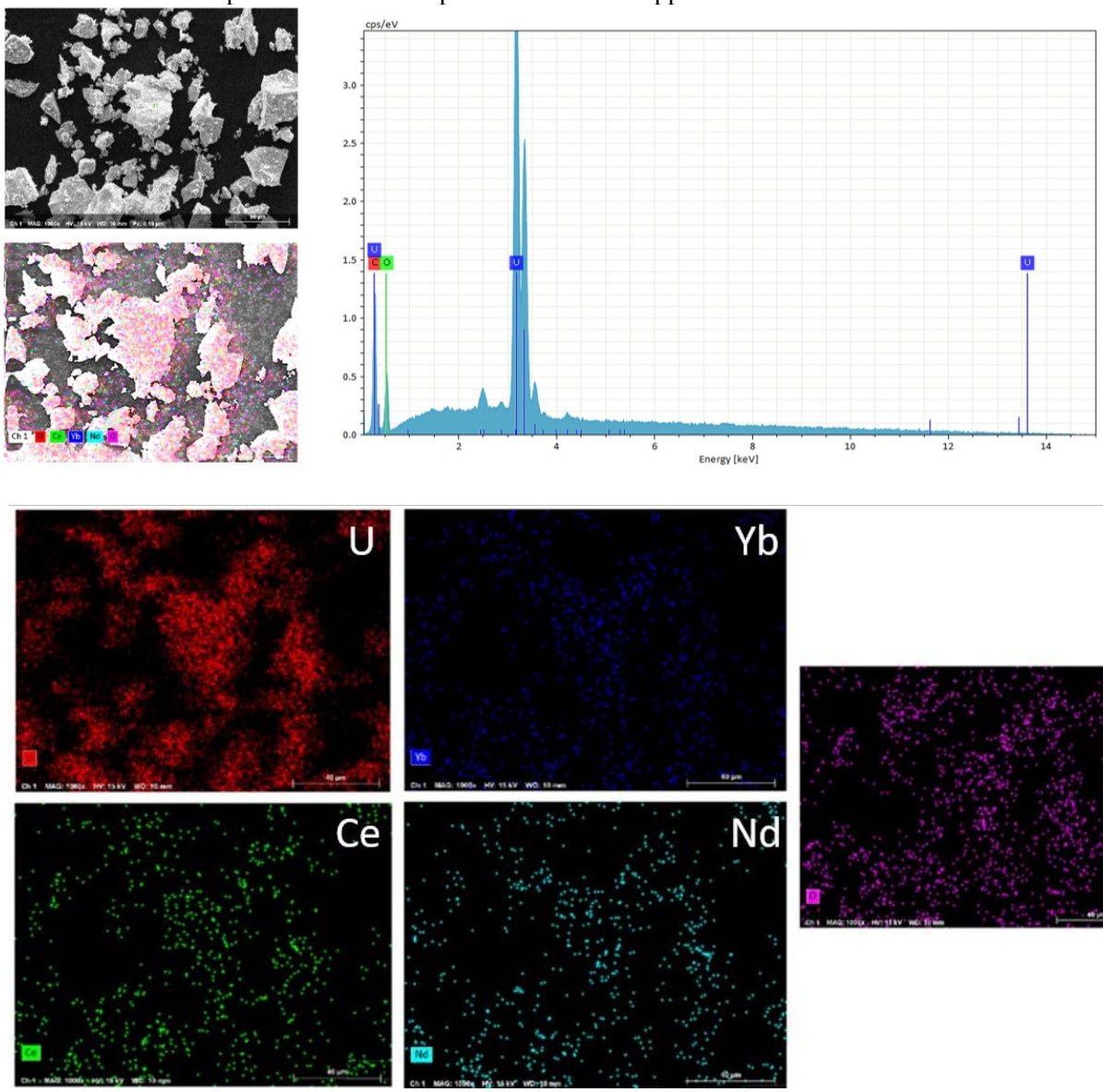

Figure B-1. EDS results of pure UO_2 pre-dissolution.

Table B-1. EDS results and relative error from 1% Ce-doped UO_2.

Element	Normalized Mass %	Relative Error % (1σ)
U	88.87	3.12
C	6.08	14.36
O	5.05	18.54

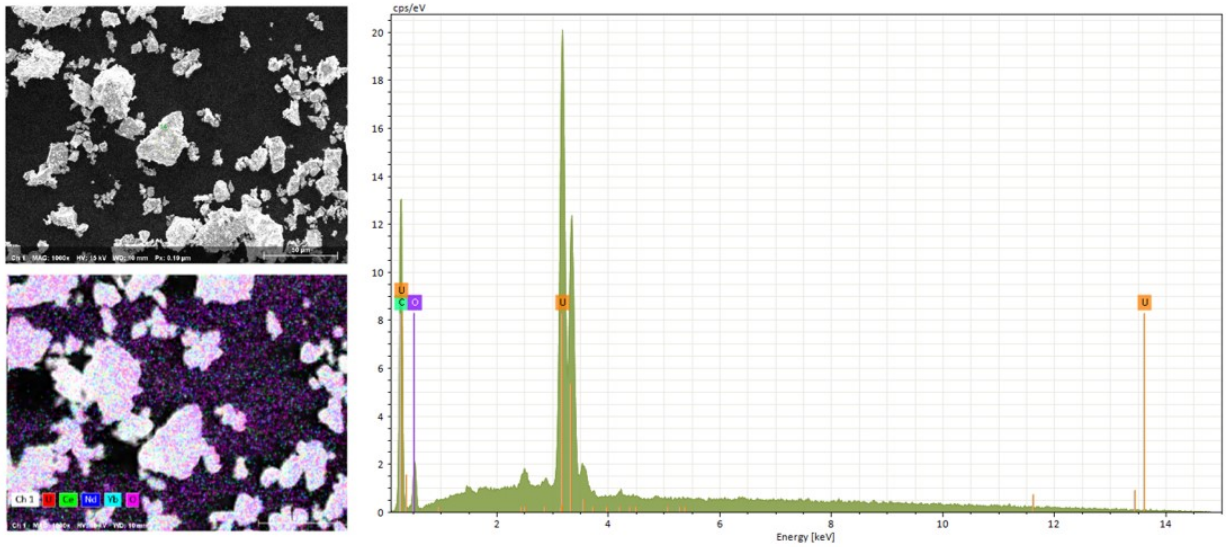

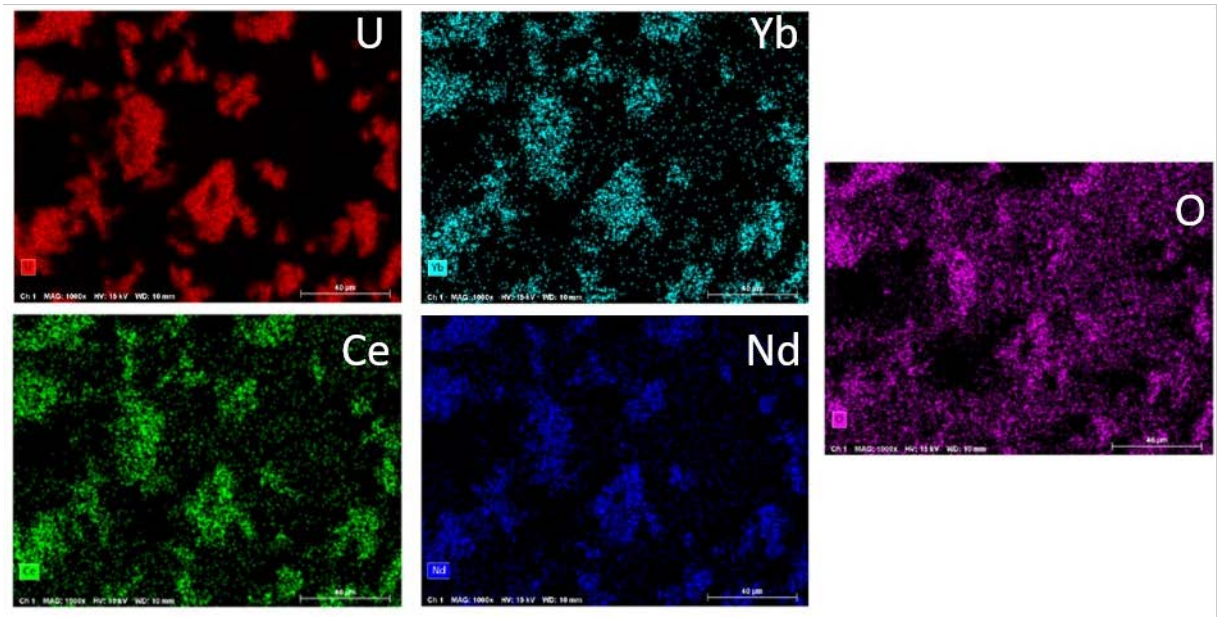

Figure B-2. EDS results of 1% Ce-doped UO_2 pre-dissolution.

Table B-2. EDS results and error from 5% Ce-doped UO_2.

Element	Normalized Mass %	Relative Error % (1σ)
U	86.33	3.15
C	6.59	15.15
O	6.39	19.21
Ce	0.69	10.49

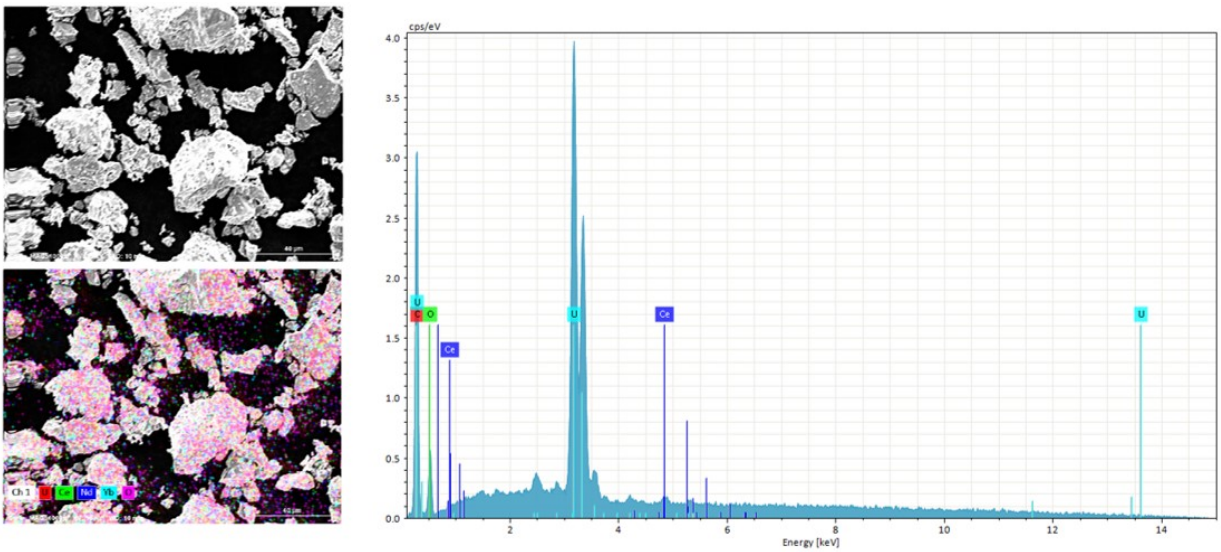

Figure B-3. EDS results of 5% Ce-doped UO_2 pre-dissolution.

Table B-3. EDS results and error from 1% Nd-doped UO_2.

Element	Normalized Mass %	Relative Error % (1σ)
U	86.32	3.26
C	4.37	21.16
O	6.40	25.66
Mg	2.91	8.35

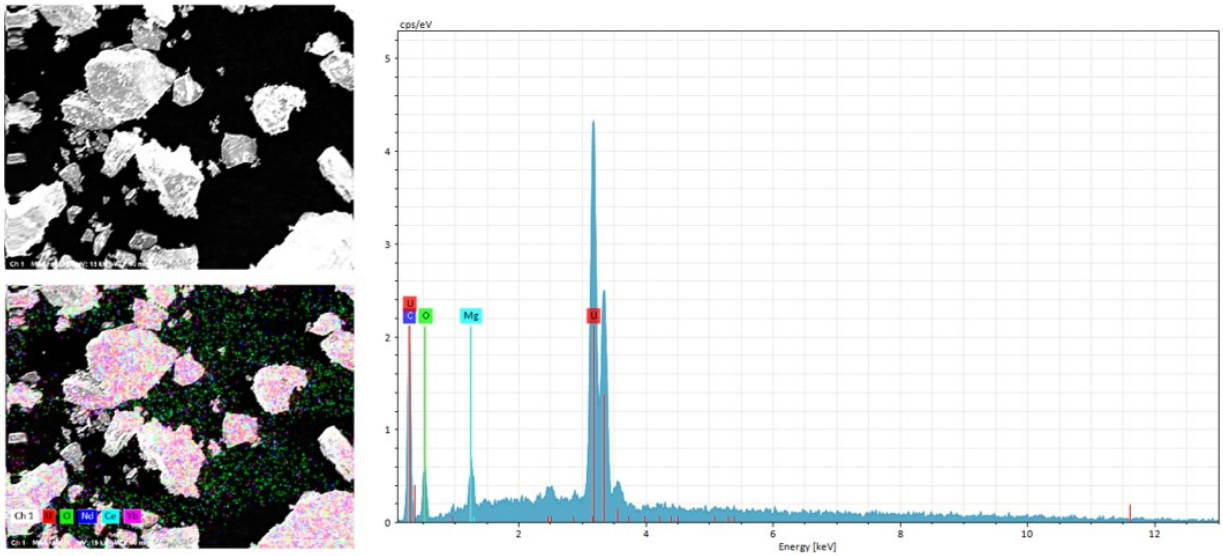

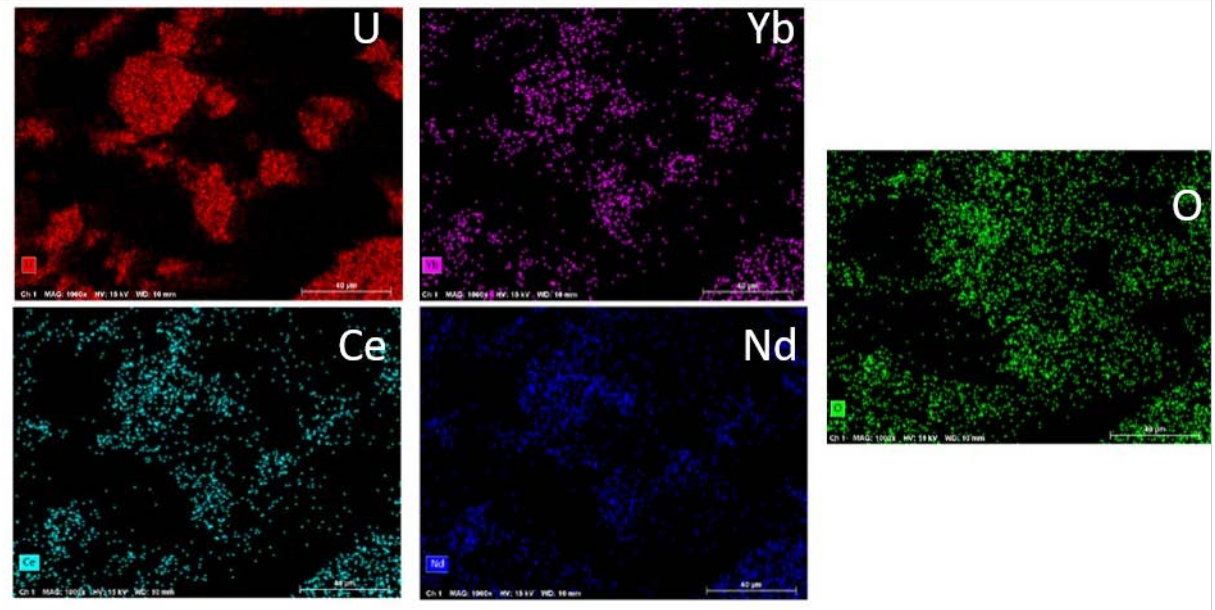

Figure B-4. EDS results of 1% Nd-doped UO_2 pre-dissolution.

Table B-4. EDS results and error from 5% Nd-doped UO_2.

Element	Normalized Mass %	Relative Error % (1σ)
U	80.67	3.22
C	9.67	16.14
O	5.76	24.06
Nd	3.23	6.23
Mg	0.68	13.57

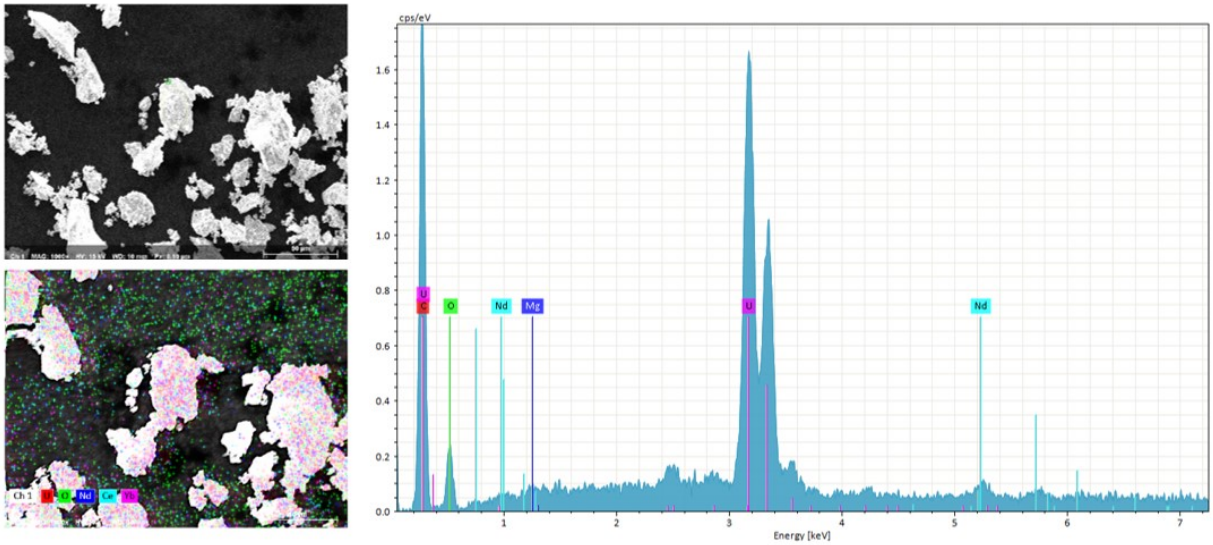

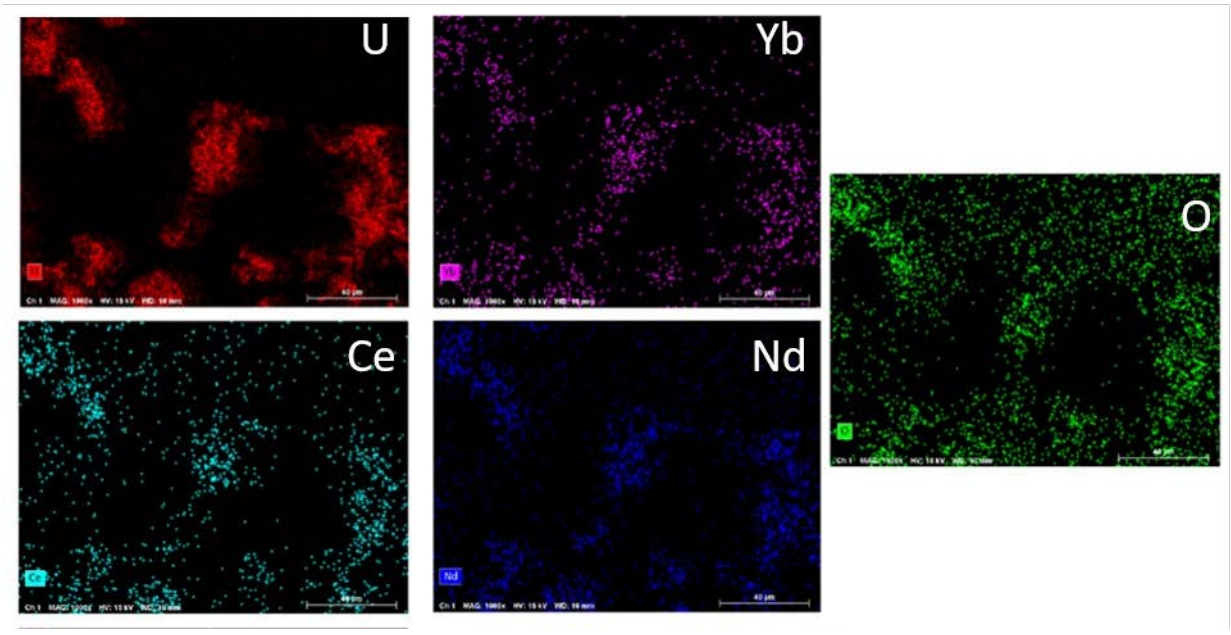

Figure B-5. EDS results of 5% Nd-doped UO_2 pre-dissolution.

Table B-5. EDS results and error from 1% Yb-doped UO_2.

Element	Normalized Mass %	Relative Error % (1σ)
U	89.53	3.21
C	4.37	19.25
O	6.10	23.91

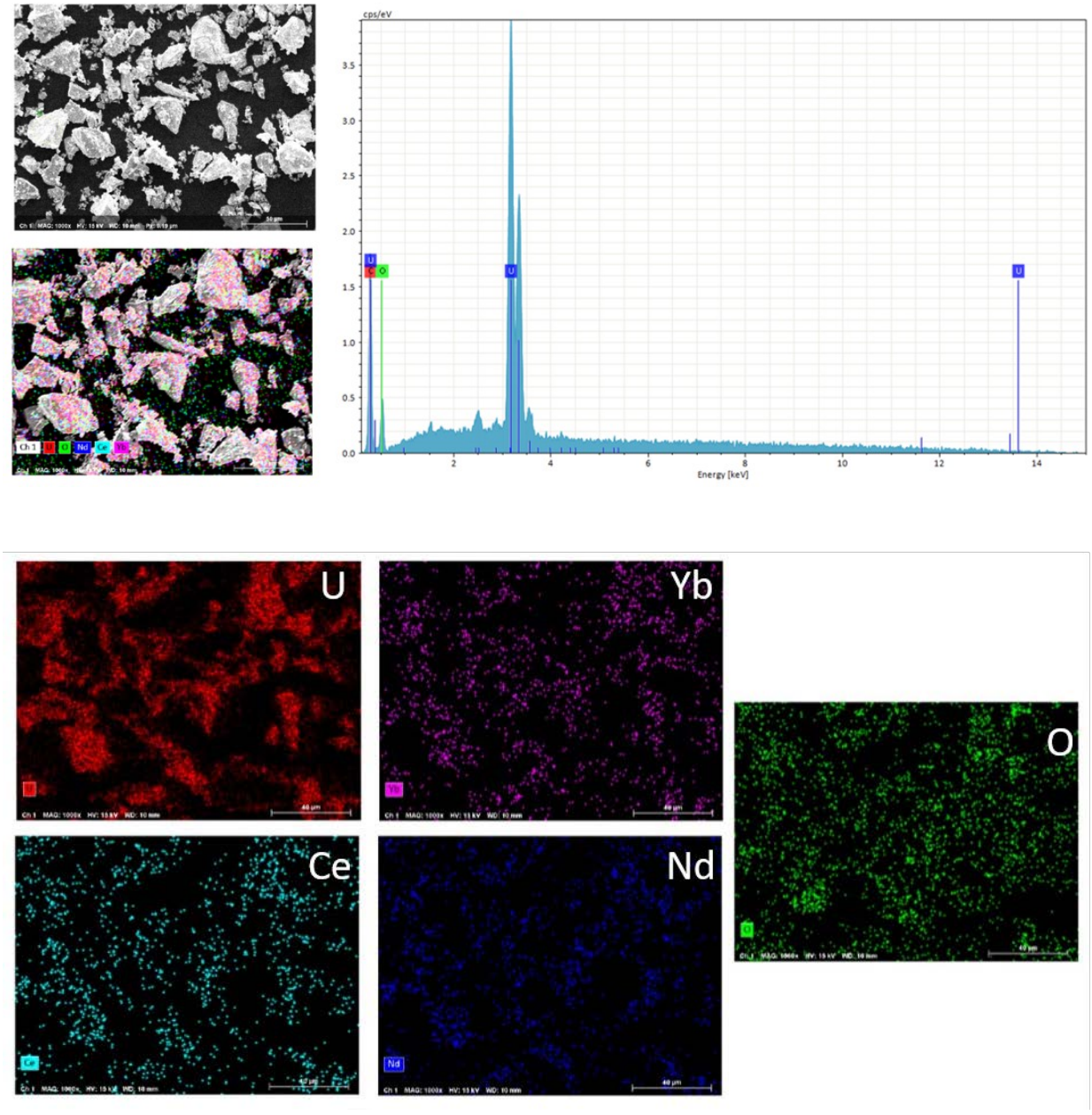

Figure B-6. EDS results of 1% Yb-doped UO_2 pre-dissolution.

Table B-6. EDS results and error from 5% Yb-doped UO_2.

Element	Normalized Mass %	Relative Error % (1σ)
U	90.11	3.13
O	4.74	20.05
Yb	3.26	6.02
C	1.89	19.66

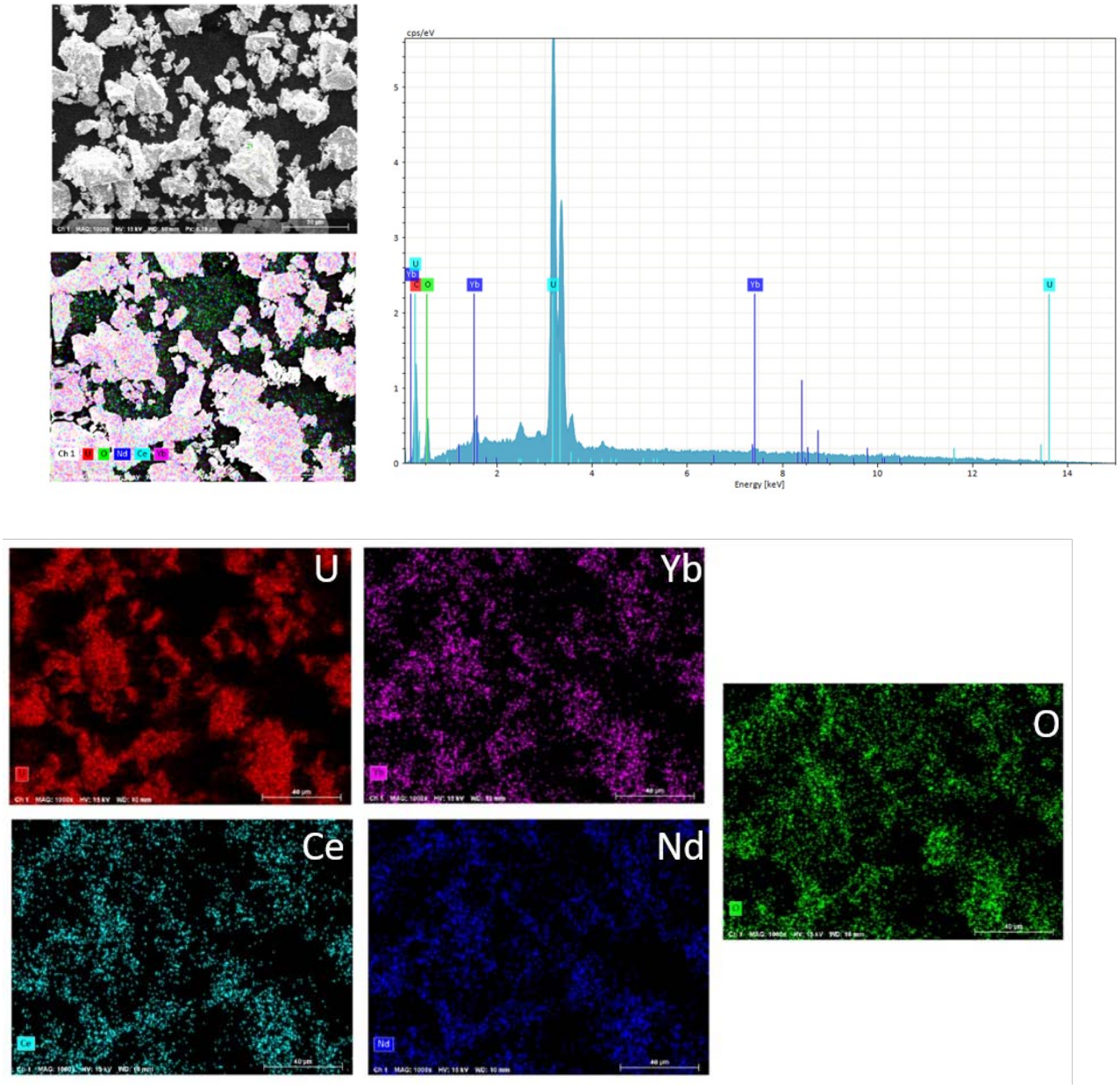

Figure B-7. EDS results of 5% Yb-doped UO_2 pre-dissolution.

This page is intentionally left blank.

Appendix C

Table C-1. Post-dissolution EDS surface content measurements.

Column \ Element (Norm. Mass %)	C	O	U	Ce	Nd	Yb	Other
A1 – Pure UO_2 Powder	2.31	4.05	93.65	ND	ND	ND	ND
A2 – 1% Ce-doped Powder	1.70	4.63	93.67	ND	ND	ND	ND
A3 – 5% Ce-doped Powder	1.53	1.82	96.66	ND	ND	ND	ND
A4 – 1% Nd-doped Powder	1.92	3.33	94.77	ND	ND	ND	ND
A5 – 5% Nd-doped Powder	1.39	4.29	88.78	ND	5.53	ND	ND
A6 – 1% Yb-doped Powder	1.30	2.33	96.36	ND	ND	ND	ND
A7 – 5% Yb-doped Powder	1.32	3.18	90.44	ND	ND	4.76	Ni – 0.62
A8 – 5% Ce-doped Fragments	1.35	2.09	93.63	2.93	ND	ND	ND
B1 – 1% Ce-doped Powder	1.77	3.76	93.67	2.41	ND	ND	ND
B2 – Pure UO_2 Powder	1.72	2.49	95.63	ND	ND	ND	ND
B3 – 5% Ce-doped Powder	1.46	2.08	95.35	1.59	ND	ND	ND
B4 – 1% Nd-doped Powder	0.74	1.51	97.32	ND	ND	ND	Na – 2.04
B5 – 5% Nd-doped Powder	0.76	1.29	96.18	ND	3.29	ND	ND
B6 – 1% Yb-doped Powder	1.75	2.38	95.35	ND	ND	ND	Al – 0.78
B7 – 5% Yb-doped Powder	4.21	3.42	93.52	ND	ND	ND	ND
B8 – 5% Ce-doped Fragments	1.32	2.31	93.86	3.46	ND	ND	Al – 0.59